Computational modeling of growth

A critical review, a classification of concepts and two new consistent approaches

E. Kuhl, A. Menzel, P. Steinmann

Abstract The present contribution is dedicated to the computational modeling of growth phenomena typically encountered in modern biomechanical applications. We set the basis by critically reviewing the relevant literature and classifying the existing models. Next, we introduce a geometrically exact continuum model of growth which is not a priori restricted to applications in hard tissue biomechanics. The initial boundary value problem of biomechanics is primarily governed by the density and the deformation problem which render a nonlinear coupled system of equations in terms of the balance of mass and momentum. To ensure unconditional stability of the required time integration procedure, we apply the classical implicit Euler backward method. For the spatial discretization, we suggest two alternative strategies, a node-based and an integration point–based approach. While for the former, the discrete balance of mass and momentum are solved simultaneously on the global level, the latter is typically related to a staggered solution with the density treated as internal variable. The resulting algorithms of the alternative solution techniques are compared in terms of stability, uniqueness, efficiency and robustness. To illustrate their basic features, we elaborate two academic model problems and a typical benchmark example from the field of biomechanics.

Keywords Growth, Bone remodeling, Finite element technologies, Stability, Convergence

1
Introduction

Since the formulation of the first continuum model of growth which was presented more than a quarter of a century ago by Cowin and Hegedus [8], the modeling and simulation of biomechanical processes has experienced an enormously growing interest. In contrast to traditional engineering materials, biomaterials, in particular hard and soft tissues, show the ability to adapt not only their external shape but also their internal microstructure to environmental changes. The functional adaption of hard tissues to changes in the mechanical loading situation has been known for more than a century and is often referred to as Wolff's law of bone remodeling [53]. Comprehensive

E. Kuhl, A. Menzel, P. Steinmann (✉)
Chair of Applied Mechanics, University of Kaiserslautern,
P.O. Box 3049, D-67653 Kaiserslautern, Germany
e-mail: ps@rhrk.uni-kl.de

overviews on the experimental findings of growth phenomena can be found e.g. in the monographs of Pauwels [45], Fung [12, 13], Taber [48], Carter and Beaupré [2] and Humphrey [27].

The first continuum theory of growth for hard tissues has been presented under the name of theory of adaptive elasticity by Cowin and Hegedus [8]. Within their theory, the biological structure is considered as an open system which is allowed to constantly exchange mass, momentum, energy and entropy with its environment. While this exchange is accounted for exclusively in terms of volume source terms in the original model, the more enhanced model by Epstein and Maugin [10] additionally allows for an exchange in terms of surface fluxes, see also Kuhl and Steinmann [31]. Thereby, the flux of mass is typically attributed to the migration of cells while mass sources stem from cell growth and shrinkage, cell death, cell division or cell enlargement. A completely different approach to hard and soft tissue mechanics falls within the framework of the theory of porous media, see e.g. Ehlers and Markert [9], Kühn and Hauger [36], Humphrey and Rajagopal [27] or Steeb and Diebels [47]. Thereby, the exchange of mass, momentum, energy and entropy takes place between the individual constituents of the mixture, while the mass, momentum, energy and entropy of the overall mixture remain constant. Nevertheless, since the mechanical behavior of hard tissues is primarily governed by the response of the calcified bone matrix, we shall confine attention to the solid phase alone and make use of the open system framework in the sequel.

Driven by the development of modern computer technologies, the newly derived theories of growth were soon supplemented by finite element based numerical simulations. Although the initial class of models suffered from numerical instabilities, the first results in the area of bone remodeling were quite encouraging, see e.g. Huiskes et al. [24, 26], Carter et al. [4], Beaupré et al. [1], Weinans et al. [49, 50] or Harrigan and Hamilton [17, 18] or the recent overview by Hart [21]. However, these first models were basically restricted to the mechanics of hard tissues such as bones. In contrast to hard tissues, which are typically not subjected to large strains, the modeling of soft tissues requires a geometrically nonlinear kinematic description, see e.g. the first publication by Rodriguez et al. [46] or the recent works of Cowin [6], Holzapfel et al. [22], Chen and Hoger [5], Gasser and Holzapfel [14] and Lubarda and Hoger [40].

The first attempts of our own group to simulate biological growth processes within the geometrically exact

framework are documented in Kuhl and Steinmann [31–35]. In the present work, we focus on the comparison of different finite element techniques for biomechanical growth processes. In particular, two alternative classes of models will be derived and elaborated: a node-based and an integration point–based approach. While the former is based on the monolithic solution of the balance of mass and momentum for open systems and offers the potential to incorporate a mass flux, the latter is based on a staggered solution strategy by introducing the density as internal variable on the quadrature point level. In view of modern finite element technologies, both approaches will be combined with a fully implicit Euler backward time integration scheme and are embedded in an incremental iterative Newton-Raphson solution technique supplemented by a consistent linearization of the governing equations. Rather than analyzing the features of the suggested approaches in fully three-dimensional applications as done by Kuhl and Steinmann [34], we shall focus on the systematic study of one-dimensional model problems and on the analysis of the classical two-dimensional benchmark problem of the proxima femur in the present contribution.

This contribution is organized as follows. We set the stage by reviewing the existing literature on finite element based numerical modeling of growth in Chapter 2. Chapter 3 then introduces the basic equations of growth within the framework of finite strain kinematics. The corresponding finite element formulation is derived in Chapters 4 and 5, whereby the former focuses on a node-based approach while the latter is characterized through an integration point–based treatment of the density. Both finite element chapters incorporate the spatial discretization, the consistent linearization, a characteristic flow-chart of the algorithm and the discussion of two academic model problems. The applicability of the two different classes of solution strategies to a classical example from biomechanics is studied in Chapter 6. Chapter 7 presents a final discussion of the derived results.

2
Different remodeling algorithms revised
We begin our study with a review of the existing literature on the computational modeling of growth which dates back to the mid eighties. Surprisingly, an enormous body of literature is related to the analysis of stability and uniqueness of the suggested models. Often, these properties are attributed to the final finite element solution although they typically originate from the ill-posedness of the underlying continuous problem. To clarify the notions of stability and uniqueness, we shall make a clear distinction between the continuous problem, the time-discrete problem and the fully discrete finite element problem.

2.1
Stability and uniqueness of continuous model
The modeling of growth is basically characterized through two fundamental equations: the balance of mass and the balance of momentum. While the computational treatment of the balance of momentum, i.e. the deformation

problem, is rather standard in modern finite element technologies, the numerical solution of the balance of mass, i.e. the density problem, can be carried out in various different ways. Conceptually speaking, the evolution of the material density has to be calculated according to some driving force, the so-called biological stimulus. After analyzing different mechanically induced stimuli, e.g. based on the current strain [8], the actual stress state [4] or the dissipated energy in the form of damage [39], it was agreed upon, that the free energy density of the calcified tissue represented the most reasonable candidate. [29, 30, 49, 50]. However, it soon turned out, that the use of the free energy density alone resulted in instabilities due to the positive feedback effect it had on the remodeling process. As documented by Carter et al. [4], Harrigan and Hamilton [16–19], Harrigan et al. [20] and Weinans et al. [49] it produced unstable 0–1-type solutions of either no bone or fully dense calcified bone which were physically meaningless. Several different remedies were suggested, e.g. the introduction of a so-called dead-zone [1, 2, 50], the non-local averaging based on spatial influence functions [41, 42], the a posteriori smoothing of either the mechanical stimulus or the solution itself [11, 28, 43, 44] or the use of more sophisticated micromechanically motivated models [23, 25]. Nevertheless, the simplest and maybe also most efficient modification was motivated by pure mathematical reasoning. In a rigorous analysis on stability and uniqueness, Harrigan and Hamilton [17, 18] derived a modified remodeling rate equation which a priori guaranteed stable, unique and path-independent solutions for a particular choice of parameters. We shall thus apply a biomechanical stimulus in the sense of Harrigan and Hamilton in the sequel.

2.2
Stability and uniqueness of semi-discrete model
The resulting set of equations defines the continuous initial boundary value problem which has to be discretized in time and space. Traditionally, finite difference schemes are applied for the temporal discretization. Motivated by the computational efficiency of explicit time integration schemes, the first models were based on the classical explicit Euler forward method, see e.g. [1, 4, 26, 49, 50]. In contrast to the unconditionally stable implicit Euler backward scheme, the Euler forward method is only conditionally stable and poses restrictions on the time step size. These were discussed in detail by Levenston [37, 38] and Cowin et al. [7]. However, we do not believe, that the use of an explicit time marching scheme is the source, at least not the only one, for the particular instabilities reported in the literature. Nevertheless, to avoid this potential drawback of explicit schemes, Harrigan and Hamilton [17] suggested the use of the Euler backward method which was also applied by Nackenhorst [43, 44] and will be the method of choice for our further deviations.

2.3
Stability and uniqueness of fully discrete model
The temporal discretization renders a highly nonlinear semi-discrete coupled system of equations. Its spatial

discretization is usually embedded in the finite element framework. Upon all the existing finite element solution strategies, we can basically distinguish three different approaches to evaluate the balance of mass and momentum: a partitioned sequential solution, the partitioned staggered solution and the monolithic simultaneous solution. Most of the pioneering work falls within the first category, see e.g. Huiskes et al. [24, 26], Carter et al. [4], Beaupré et al. [1] or Weinans et al. [49, 50]. Driven by the need for computational efficiency that was a relevant issue in the mid eighties, the solution was traditionally carried out in a two-step-strategy. First, the balance of momentum was solved in the classical way. Only then, the density was determined in a mere post-processing step. The constitutive properties were adjusted according to the current density and a new set of material parameters was assigned to each element before the next iteration step was carried out. The structure of the applied commercial finite element codes basically prescribed the algorithmic setup. Since the density was assumed to be elementwise constant within this algorithm, this first strategy has been termed element-based approach in the literature.

Unfortunately, most of the simulations of the element-based approach produced unphysical checkerboard-type solutions which were attributed to the fact that the density was interpolated in a $\mathscr{C}^{-1}$-continuous fashion. This deficiency of the original models led to the reconsideration of the finite element realization in the mid nineties. In a systematic case study, Jacobs et al. [28] compared the early element-based approach with an integration point-based approach and a node-based approach. For the integration point-based approach, the balance of mass and momentum are still elaborated in a partitioned way, however, their evaluation is carried out in a staggered sense, see also Weng [52]. In the integration point-based approach, which originates back to the computational modeling of inelasticity, the density is introduced as an internal variable on the integration point level. Nevertheless, since the integration point-based approach is still based on a discrete pointwise representation of the density field, it did not yield any remarkable improvements.

If the density field is assumed to be at least $\mathscr{C}^0$-continuous within the entire domain of consideration, the density has to be introduced as nodal degree of freedom on the global level. According to Jacobs et al. [28] and Fischer et al. [11], only this node-based approach could guarantee a physically meaningful solution. In complete analogy to the temperature field in thermo-elastic problems, the density is treated as an independent field which can be determined simultaneously with the deformation field. The monolithic solution of the balance of mass and momentum is computationally more expensive; thus it is not surprising that this solution strategy only became prominent after sufficient computational facilities had become available.

Within the present work, we shall derive a class of node-based and integration point-based finite element formulations, which are based on a monolithic simultaneous and on a partitioned staggered solution strategy, respectively. However, it will turn out, that the approach that had been termed element-based in the literature can be understood as a special case of either of the two categories. We will illustrate, that, provided that the spatial discretization is carried out in a consistent way, neither of the three approaches leads to unstable solutions if the underlying continuous problem is stable and unique in the sense of Harrigan and Hamilton [16–18].

3
Theory of growth

Within the present chapter, we introduce the basic equations of the continuum theory of growth: the fundamental kinematics, the relevant balance equations and the constitutive assumptions. To lay the basis for the finite element formulations derived in the following chapters, we cast the governing equations into their weak format which is then discretized in time.

3.1
Kinematics

To set the stage, we briefly summarize the underlying kinematics of geometrically nonlinear continuum mechanics. Let $\mathscr{B}_0$ and $\mathscr{B}_t$ denote the reference and current configuration occupied by the body of interest at time t_0 and $t \in \mathbb{R}$, respectively. The kinematic description is basically characterized through the deformation map $\boldsymbol{\varphi}$ mapping the material placement $\mathbf{x}$ of a physical particle in the material configuration $\mathscr{B}_0$ to its spatial placement $\mathbf{X}$ in the spatial configuration $\mathscr{B}_t$.

$$\mathbf{x} = \boldsymbol{\varphi}(\mathbf{X}, t): \quad \mathscr{B}_0 \times \mathbb{R} \rightarrow \mathscr{B}_t \tag{1}$$

The corresponding deformation gradient $\mathbf{F}$ defines the linear tangent map from the material tangent space $T\mathscr{B}_0$ to the spatial tangent space $T\mathscr{B}_t$.

$$\mathbf{F} = \nabla\boldsymbol{\varphi}(\mathbf{X}, t): \quad T\mathscr{B}_0 \rightarrow T\mathscr{B}_t \tag{2}$$

Its determinant defines the related Jacobian J as $J = \det \mathbf{F} > 0$. Moreover, we introduce the left Cauchy–Green tensor $\mathbf{b} = \mathbf{F} \cdot \mathbf{F}^t$ as a characteristic spatial strain measure. In what follows, $D_t = \partial_t\{\bullet\}|_X$ will denote the material time derivative of a quantity $\{\bullet\}$ at fixed material placement $\mathbf{X}$. Accordingly, the spatial velocity $\mathbf{v} = D_t\boldsymbol{\varphi}(\mathbf{X}, t)$ can be understood as the material time derivative of the deformation map $\boldsymbol{\varphi}$. Recall, that its material gradient $\nabla\mathbf{v}$ is identical to the material time derivative of the deformation gradient $\mathbf{F}$ as $D_t\mathbf{F} = \nabla\mathbf{v}$. In the sequel, we shall apply a formulation which is entirely related to the material frame of reference. Thus, $\nabla\{\bullet\}$ and $\text{Div}\{\bullet\}$ denote the gradient and the divergence of any field $\{\bullet\}$ with respect to the material placement $\mathbf{X}$.

3.2
Balance equations

Having introduced the basic kinematic quantities, we now turn to the discussion of the balance equations for the mechanics of growth. While in classical continuum mechanics the amount of matter contained in a fixed reference volume $\mathscr{B}_0$ typically does not change no matter how the body is moved, deformed or accelerated, the density ρ_0 of the reference body no longer represents a conservation property within the theory of growth. Rather, its rate of

change is determined by a possible in- or outflux of mass $\mathbf{R}$ and an amount of locally created material $\mathcal{R}_0$.

$$\mathrm{D}_t \rho_0 = \mathrm{Div}\,\mathbf{R} + \mathcal{R}_0 \tag{3}$$

In a similar way, the balance of momentum balances the weighted rate of change of the mass-specific momentum density $\mathbf{p}$ which is nothing but the spatial velocity $\mathbf{p} = \mathrm{D}_t \boldsymbol{\varphi}(\mathbf{X}, t) = \mathbf{v}$ with the reduced momentum flux $\bar{\boldsymbol{\Pi}}^t$ and the reduced momentum source $\bar{\mathbf{b}}_0$.

$$\rho_0 \mathrm{D}_t \mathbf{p} = \mathrm{Div}\,\bar{\boldsymbol{\Pi}}^t + \bar{\mathbf{b}}_0 \tag{4}$$

Note, that the above equation represents the so-called 'mass-specific' version of the balance of momentum which is particularly useful in the context of growth since it contains no explicit dependence on changes in mass. The nature of growth thus manifests itself exclusively in terms of the Neumann boundary conditions for the reduced momentum flux $\bar{\boldsymbol{\Pi}}^t \cdot \mathbf{N} = \mathbf{t}^{\mathrm{closed}} + \bar{\mathbf{t}}^{\mathrm{open}}$ and the definition of the reduced momentum source $\bar{\mathbf{b}}_0 = \mathbf{b}_0^{\mathrm{closed}} + \bar{\mathbf{b}}_0^{\mathrm{open}}$ in which the additional growth-dependent contributions $\bar{\mathbf{t}}^{\mathrm{open}}$ and $\bar{\mathbf{b}}_0^{\mathrm{open}}$ are taken into account. A detailed derivation of the balance equations for the mechanics of growth within the framework of open system thermodynamics can be found in Kuhl and Steinmann [31, 35].

Remark 3.1 Within the classical literature of biomechanics, the balance of mass (3) is typically referred to as 'biological' or 'homeostatic equilibrium' while the balance of momentum (4) represents the equation of 'mechanical equilibrium'.

3.3
Constitutive equations
Finally, the set of governing equations has to be closed by introducing appropriate constitutive assumptions for the mass flux $\mathbf{R}$, the mass source $\mathcal{R}_0$, the reduced momentum flux $\bar{\boldsymbol{\Pi}}^t$ and the reduced momentum source $\bar{\mathbf{b}}_0$. Paralleling the definition of the flux of concentrations according to Fick's law, the mass flux $\mathbf{R}$

$$\mathbf{R} = R_0 \nabla \rho_0 \tag{5}$$

is related to the gradient of the density $\nabla \rho_0$ weighted by a mass conduction coefficient R_0 whereby the latter has the unit of a length squared divided by the time. Following Harrigan and Hamilton [17, 18], we propose a constitutive equation for the mass source $\mathcal{R}_0$ which is governed by the free energy $\Psi_0 = \rho_0 \Psi$.

$$\mathcal{R}_0 = c\left[\left[\frac{\rho_0}{\rho_0^*}\right]^{-m}\Psi_0 - \Psi_0^*\right] \tag{6}$$

Herein, ρ_0^* and Ψ_0^* denote the reference value of the density and of the free energy, respectively, while m is an additional material parameter. Moreover, the additional parameter c, which is of the unit time divided by the length squared, basically governs the speed of the adaption process. In the context of hard tissue mechanics, the free energy Ψ_0 is typically characterized through the elastic free energy, e.g. of Neo-Hooke type $\Psi_0^{\mathrm{neo}} = \left[\lambda \ln^2 J + \mu[\mathbf{b} : \mathbf{1} - 3 - 2\ln J]\right]/2$, weighted by the relative density $[\rho_0/\rho_0^*]^n$ such that $\Psi_0 = [\rho_0/\rho_0^*]^n \Psi_0^{\mathrm{neo}}$, see e.g. Carter and Hayes [3] or Gibson and Ashby [15].

Herein, λ and μ are the classical Lamé constants. Moreover, the exponent n typically varies between $1 \leq n \leq 3.5$ according to the actual porosity of the open-pored ground substance. This particular choice of the free energy defines the reduces momentum flux as $\bar{\boldsymbol{\Pi}}^t = \rho_0 \mathrm{D}_F \Psi$.

$$\bar{\boldsymbol{\Pi}}^t = \left[\frac{\rho_0}{\rho_0^*}\right]^n \bar{\boldsymbol{\Pi}}^{\mathrm{neo}\, t} \tag{7}$$

with $\bar{\boldsymbol{\Pi}}^{\mathrm{neo}\, t} = [\mu \mathbf{F} + [\lambda \ln J - \mu]\mathbf{F}^{-t}]$. The reduced momentum flux $\bar{\boldsymbol{\Pi}}^t$ can thus be interpreted as the classical Neo-Hookean first Piola Kirchhoff stress tensor $\bar{\boldsymbol{\Pi}}^{\mathrm{neo}\, t}$ weighted by the actual relative density $[\rho_0/\rho_0^*]^n$. For the sake of simplicity, the reduced momentum source $\bar{\mathbf{b}}_0$ is assumed to vanish identically.

$$\bar{\mathbf{b}}_0 = \mathbf{0} \tag{8}$$

Remark 3.2 The introduction of a mass flux has been studied in detail by Kuhl and Steinmann [33]. Note, however, that the incorporation of a mass flux which essentially smoothes sharp solutions and enables the simulation of size effects requires at least a $\mathscr{C}^0$-continuous interpolation of the density corresponding to its discretization as global unknown on the nodal level.

Remark 3.3 In the context of biomechanics, the driving force of the evolution of mass is classically referred to as 'biological stimulus'. Herein, we have suggested a free-energy based stimulus of the form $[\rho_0/\rho_0^*]^{-m}\Psi_0$. Correspondingly, the reference free energy Ψ_0^* can be understood as 'attractor stimulus'. However, alternative stress- or strain based stimuli as discussed e.g. by Weinans and Prendergast [51]. Even energy-dissipation based stimuli can be found in the recent literature, see e.g. Levenston and Carter [39].

Remark 3.4 The choice of the exponent m determines the stability of the resulting algorithm. With $m = 1$ we obtain the classical model of Beaupré et al. [1]. Nevertheless, Harrigan and Hamilton [17, 18] choose $m > n$ to guarantee uniqueness and stability of the solution.

3.4
Strong form
The reference density ρ_0 and the deformation $\boldsymbol{\varphi}$ furnish the primary unknowns of the mechanics of growth. They are governed by the scalar-valued balance of mass (3) and by the vector-valued mass-specific balance of momentum (4) which can be cast into the residual statements

$$\begin{aligned} \mathrm{R}^\rho(\rho_0, \boldsymbol{\varphi}) &= 0 \quad \text{in } \mathscr{B}_0 \\ \mathbf{R}^\varphi(\rho_0, \boldsymbol{\varphi}) &= \mathbf{0} \quad \text{in } \mathscr{B}_0 \end{aligned} \tag{9}$$

with the residuals R^ρ and $\mathbf{R}^\varphi$ defined in the following form.

$$\begin{aligned} \mathrm{R}^\rho &= \mathrm{D}_t \rho_0 \quad - \mathrm{Div}\,\mathbf{R} \quad - \mathcal{R}_0 \\ \mathbf{R}^\varphi &= \rho_0 \mathrm{D}_t \mathbf{p} - \mathrm{Div}\,\bar{\boldsymbol{\Pi}}^t - \bar{\mathbf{b}}_0 \end{aligned} \tag{10}$$

Herein, the boundary $\partial \mathscr{B}_0$ of the material domain can be decomposed into disjoint parts $\partial \mathscr{B}_0^\rho$ and $\partial \mathscr{B}_0^r$ for the

density problem and equivalently into $\partial\mathscr{B}_0^\varphi$ and $\partial\mathscr{B}_0^t$ for the deformation problem. While Dirichlet boundary conditions are prescribed on $\partial\mathscr{B}_0^\rho$ and $\partial\mathscr{B}_0^\varphi$,

$$\rho_0 - \rho_0^{\text{presc}} = 0 \quad \text{on } \partial\mathscr{B}_0^\rho$$
$$\boldsymbol{\varphi} - \boldsymbol{\varphi}^{\text{presc}} = \mathbf{0} \quad \text{on } \partial\mathscr{B}_0^\varphi \tag{11}$$

Neumann boundary conditions can be given for the mass flux and the tractions on $\partial\mathscr{B}_0^r$ and $\partial\mathscr{B}_0^t$,

$$\mathbf{R} \cdot \mathbf{N} - [r^{\text{closed}} + \bar{r}^{\text{open}}] = 0 \quad \text{on } \partial\mathscr{B}_0^r$$
$$\bar{\boldsymbol{\Pi}}^t \cdot \mathbf{N} - [\mathbf{t}^{\text{closed}} + \bar{\mathbf{t}}^{\text{open}}] = \mathbf{0} \quad \text{on } \partial\mathscr{B}_0^t \tag{12}$$

with $\mathbf{N}$ denoting the outward normal to $\partial\mathscr{B}_0$.

3.5
Weak form

As a prerequisite for the finite element discretization, the coupled set of equations has to be reformulated in weak form. To this end, the residual statements of the balance of mass and momentum (9) and the corresponding Neumann boundary conditions (12) are tested by the scalar- and vector-valued test function $\delta\rho$ and $\delta\boldsymbol{\varphi}$, respectively.

$$G^\rho(\delta\rho; \rho_0, \boldsymbol{\varphi}) = 0 \quad \forall \delta\rho \quad \text{in } H_1^0(\mathscr{B}_0)$$
$$G^\varphi(\delta\boldsymbol{\varphi}; \rho_0, \boldsymbol{\varphi}) = 0 \quad \forall \delta\boldsymbol{\varphi} \quad \text{in } H_1^0(\mathscr{B}_0) \tag{13}$$

The weak forms G^ρ and G^φ expand into the following expressions.

$$G^\rho = \int_{\mathscr{B}_0} \delta\rho \mathrm{D}_t\rho_0 \, \mathrm{d}V + \int_{\mathscr{B}_0} \nabla\delta\rho \cdot \mathbf{R} \, \mathrm{d}V$$
$$- \int_{\partial\mathscr{B}_0^r} \delta\rho[r^{\text{closed}} + \bar{r}^{\text{open}}]\mathrm{d}A - \int_{\mathscr{B}_0} \delta\rho\mathscr{R} \, \mathrm{d}V$$

$$G^\varphi = \int_{\mathscr{B}_0} \delta\boldsymbol{\varphi} \cdot \rho_0 \mathrm{D}_t\mathbf{p} \, \mathrm{d}V + \int_{\mathscr{B}_0} \nabla\delta\boldsymbol{\varphi} : \bar{\boldsymbol{\Pi}}^t \, \mathrm{d}V$$
$$- \int_{\partial\mathscr{B}_0^t} \delta\boldsymbol{\varphi} \cdot [\mathbf{t}^{\text{closed}} + \bar{\mathbf{t}}^{\text{open}}]\mathrm{d}A - \int_{\mathscr{B}_0} \delta\boldsymbol{\varphi} \cdot \bar{\mathbf{b}}_0 \, \mathrm{d}V \tag{14}$$

3.6
Temporal discretization

For the temporal discretization of the governing equations (13), we partition the time interval of interest $\mathscr{T}$ into n_{step} subintervals $[t_n, t_{n+1}]$ as

$$\mathscr{T} = \bigcup_{n=0}^{n_{\text{step}}-1} [t_n, t_{n+1}] \tag{15}$$

and focus on a typical time slab $[t_n, t_{n+1}]$ for which $\Delta t := t_{n+1} - t_n > 0$ denotes the actual time increment. Assume, that the primary unknowns ρ_{0n} and $\boldsymbol{\varphi}_n$ and all derivable quantities are known at the beginning of the actual subinterval t_n. In the spirit of implicit time marching schemes, we now reformulate the set of governing equations in terms of the unknowns ρ_{0n+1} and $\boldsymbol{\varphi}_{n+1}$.

$$G_{n+1}^\rho(\delta\rho; \rho_{0n+1}, \boldsymbol{\varphi}_{n+1}) = 0 \quad \forall \delta\rho \text{ in } H_1^0(\mathscr{B}_0)$$
$$G_{n+1}^\varphi(\delta\boldsymbol{\varphi}; \rho_{0n+1}, \boldsymbol{\varphi}_{n+1}) = 0 \quad \forall \delta\boldsymbol{\varphi} \text{ in } H_1^0(\mathscr{B}_0) \tag{16}$$

Without loss of generality, we shall apply the classical Euler backward time integration scheme in the sequel. In combination with the following approximations of the first order material time derivatives $\mathrm{D}_t\rho_0$ and $\mathrm{D}_t\mathbf{p}$ as

$$\mathrm{D}_t\rho_0 = \frac{1}{\Delta t}[\rho_{0n+1} - \rho_{0n}]$$
$$\mathrm{D}_t\mathbf{p} = \frac{1}{\Delta t}[\mathbf{p}_{n+1} - \mathbf{p}_n] \tag{17}$$

we obtain the following semi-discrete weak forms of the balance of mass and momentum.

$$G_{n+1}^\rho = \int_{\mathscr{B}_0} \delta\rho \frac{\rho_{0n+1} - \rho_{0n}}{\Delta t} + \nabla\delta\rho \cdot \mathbf{R}_{n+1} \, \mathrm{d}V$$
$$- \int_{\partial\mathscr{B}_0^r} \delta\rho[r_{n+1}^{\text{closed}} + \bar{r}_{n+1}^{\text{open}}]\mathrm{d}A - \int_{\mathscr{B}_0} \delta\rho\mathscr{R}_{0n+1}\mathrm{d}V$$

$$G_{n+1}^\varphi = \int_{\mathscr{B}_0} \delta\boldsymbol{\varphi} \cdot \rho_0 \frac{\mathbf{p}_{n+1} - \mathbf{p}_n}{\Delta t} + \nabla\delta\boldsymbol{\varphi} : \bar{\boldsymbol{\Pi}}_{n+1}^t \, \mathrm{d}V$$
$$- \int_{\partial\mathscr{B}_0^t} \delta\boldsymbol{\varphi} \cdot [\mathbf{t}_{n+1}^{\text{closed}} + \bar{\mathbf{t}}_{n+1}^{\text{open}}]\mathrm{d}A - \int_{\mathscr{B}_0} \delta\boldsymbol{\varphi} \cdot \bar{\mathbf{b}}_{0n+1}\mathrm{d}V \tag{18}$$

We now turn to the spatial discretization of the above set of equations. To this end, we suggest two alternative finite element techniques which differ by the treatment of the balance of mass. While the balance of mass is evaluated globally in the node-based approach, it is solved locally on the integration point-level in the second approach.

4
Node-based approach

The node-based approach derived in the present chapter is essentially characterized through a $\mathscr{C}^0$-continuous interpolation of the density field ρ_0 in combination with the standard $\mathscr{C}^0$-continuous interpolation of the deformation field $\boldsymbol{\varphi}$. Just like the displacements in classical finite element approaches, the density is introduced as a nodal degree of freedom which is solved for on the global level. This can either be done in a partitioned way by solving the balance of mass and momentum sequentially as proposed in the related literature or in a monolithic way by evaluating both balance equations simultaneously. We suggest the latter approach which is believed to be the most consistent strategy within a modern finite element context. Note, that $\mathscr{C}^0$-continuity of the density field is mandatory, if density gradients are incorporated in the formulation, e.g. through the constitutive equation of the mass flux.

4.1
Spatial discretization

In the spirit of the finite element method, the domain of interest $\mathscr{B}_0$ is discretized into n_{el} elements $\mathscr{B}_0^e$.

$$\mathscr{B}_0 = \bigcup_{e=1}^{n_{\text{el}}} \mathscr{B}_0^e \tag{19}$$

The geometry $\mathbf{X}^h$ of each subset is interpolated element-wise in terms of the local basis functions N_X and the discrete node point positions $\mathbf{X}_j$ of all $j = 1, \ldots, n_{eX}$ element nodes as $\mathbf{X}^h|_{\mathscr{B}_0^e} = \sum_{j=1}^{n_{eX}} N_X^j \mathbf{X}_j$. According to the isoparametric concept, the trial function $\boldsymbol{\varphi}^h$ is interpolated on the element level with the same basis function N_φ as the element geometry. Following the Bubnov–Galerkin approach, similar basis functions are applied to interpolate the test functions $\delta\rho^h$ and $\delta\boldsymbol{\varphi}^h$.

$$\delta\rho^h|_{\mathscr{B}_0^e} = \sum_{i=1}^{n_{e\rho}} N_\rho^i \quad \delta\rho_i \in H_1^0(\mathscr{B}_0)$$
$$\delta\boldsymbol{\varphi}^h|_{\mathscr{B}_0^e} = \sum_{j=1}^{n_{e\varphi}} N_\varphi^j \quad \delta\boldsymbol{\varphi}_j \in H_1^0(\mathscr{B}_0)$$
$$\rho_0{}^h|_{\mathscr{B}_0^e} = \sum_{k=1}^{n_{e\rho}} N_\rho^k \quad \rho_k \in H_1(\mathscr{B}_0)$$
$$\boldsymbol{\varphi}^h|_{\mathscr{B}_0^e} = \sum_{l=1}^{n_{e\varphi}} N_\varphi^l \quad \boldsymbol{\varphi}_l \in H_1(\mathscr{B}_0) \tag{20}$$

While the element set of deformation nodes $j = 1, \ldots, n_{e\varphi}$ typically corresponds to the set of node point positions $j = 1, \ldots, n_{eX}$, the element set of density nodes $i = 1, \ldots, n_{e\rho}$ can generally be chosen independently. The discretization of the gradients of the test functions $\nabla\delta\rho^h$ and $\nabla\delta\boldsymbol{\varphi}^h$ and the gradients of the trial functions $\nabla\rho^h$ and $\nabla\boldsymbol{\varphi}^h$ is straightforward and results in the following expressions.

$$\nabla\delta\rho^h|_{\mathscr{B}_0^e} = \sum_{i=1}^{n_{e\rho}} \delta\rho_i \nabla N_\rho^i$$
$$\nabla\delta\boldsymbol{\varphi}^h|_{\mathscr{B}_0^e} = \sum_{j=1}^{n_{e\varphi}} \delta\boldsymbol{\varphi}_j \otimes \nabla N_\varphi^j$$
$$\nabla\rho_0^h|_{\mathscr{B}_0^e} = \sum_{k=1}^{n_{e\rho}} \rho_k \nabla N_\rho^k$$
$$\nabla\boldsymbol{\varphi}^h|_{\mathscr{B}_0^e} = \sum_{l=1}^{n_{e\varphi}} \boldsymbol{\varphi}_l \otimes \nabla N_\varphi^l \tag{21}$$

With the above discretizations, the discrete algorithmic balance of mass and momentum can be rewritten as

$$R_I^\rho(\rho_{0_{n+1}^h}, \boldsymbol{\varphi}_{n+1}^h) = 0 \quad \forall I = 1, \ldots, n_{n\rho}$$
$$\mathbf{R}_J^\varphi(\rho_{0n+1}^h, \boldsymbol{\varphi}_{n+1}^h) = \mathbf{0} \quad \forall J = 1, \ldots, n_{n\varphi} \tag{22}$$

whereby the discrete residua R_I^ρ and $\mathbf{R}_J^\varphi$ expand into the following forms.

$$R_I^\rho = \mathbf{A}_{e=1}^{n_{\text{el}}} \int_{\mathscr{B}_0^e} N_\rho^i \frac{\rho_{0n+1} - \rho_{0n}}{\Delta t} + \nabla N_\rho^i \cdot \mathbf{R}_{n+1} \, dV$$
$$- \int_{\partial\mathscr{B}_0^{er}} N_\rho^i [r_{n+1}^{\text{closed}} + \bar{r}_{n+1}^{\text{open}}] dA - \int_{\mathscr{B}_0^e} N_\rho^i \mathscr{R}_{0n+1} dV$$

$$\mathbf{R}_J^\varphi = \mathbf{A}_{e=1}^{n_{\text{el}}} \int_{\mathscr{B}_0^e} N_\varphi^j \rho_0 \frac{\mathbf{p}_{n+1} - \mathbf{p}_n}{\Delta t} + \nabla N_\varphi^j \cdot \bar{\boldsymbol{\Pi}}_{n+1} \, dV$$
$$- \int_{\partial\mathscr{B}_0^{te}} N_\varphi^j [\mathbf{t}_{n+1}^{\text{closed}} + \bar{\mathbf{t}}_{n+1}^{\text{open}}] dA - \int_{\mathscr{B}_0^e} N_\varphi^j \bar{\mathbf{b}}_{0n+1} \, dV \tag{23}$$

Therein, the operator $\mathbf{A}$ symbolizes the assembly of all element contributions at the element density nodes $i = 1, \ldots, n_{e\rho}$ and the element deformation nodes $j = 1, \ldots, n_{e\varphi}$ to the overall residuals at the global density and deformation node points $I = 1, \ldots, n_{n\rho}$ and $J = 1, \ldots, n_{n\varphi}$.

4.2
Linearization

The discrete residual statements characterizing the mechanics of growth (22) represent a highly nonlinear coupled system of equations which can be solved efficiently within the framework of a monolithic incremental iterative Newton-Raphson solution strategy. To this end, we perform a consistent linearization of the governing equations at time t_{n+1}

$$R_{I\,n+1}^{\rho\,k+1} = R_{I\,n+1}^{\rho\,k} + dR_I^\rho \doteq 0 \quad \forall I = 1, \ldots, n_{n\rho}$$
$$\mathbf{R}_{J\,n+1}^{\varphi\,k+1} = \mathbf{R}_{J\,n+1}^{\varphi\,k} + d\mathbf{R}_J^\varphi \doteq \mathbf{0} \quad \forall J = 1, \ldots, n_{n\varphi} \tag{24}$$

whereby the iterative residua dR_I^ρ and $d\mathbf{R}_J^\varphi$ take the following format.

$$dR_I^\rho = \sum_{K=1}^{n_{n\rho}} K_{IK}^{\rho\rho} d_{\rho_K} + \sum_{L=1}^{n_{n\varphi}} \mathbf{K}_{IL}^{\rho\varphi} \cdot d\boldsymbol{\varphi}_L$$
$$d\mathbf{R}_J^\varphi = \sum_{K=1}^{n_{n\rho}} \mathbf{K}_{JK}^{\varphi\rho} d_{\rho_K} + \sum_{L=1}^{n_{n\varphi}} \mathbf{K}_{JL}^{\varphi\varphi} \cdot d\boldsymbol{\varphi}_L \tag{25}$$

In the above definitions, we have introduced the iteration matrices

$$K_{IK}^{\rho\rho} = \frac{\partial R_I^\rho}{\partial \rho_K} \quad \mathbf{K}_{IL}^{\rho\varphi} = \frac{\partial R_I^\rho}{\partial \boldsymbol{\varphi}_L}$$
$$\mathbf{K}_{JK}^{\varphi\rho} = \frac{\partial \mathbf{R}_J^\varphi}{\partial \rho_K} \quad \mathbf{K}_{JL}^{\varphi\varphi} = \frac{\partial \mathbf{R}_J^\varphi}{\partial \boldsymbol{\varphi}_L} \tag{26}$$

which take the following abstract representations.

$$K_{IK}^{\rho\rho} = \mathbf{A}_{e=1}^{n_{\text{el}}} \int_{\mathscr{B}_0^e} N_\rho^i \frac{1}{\Delta t} N_\rho^k \, dV - \int_{\mathscr{B}_0^e} N_\rho^i \partial_{\rho_0} \mathscr{R}_0 N_\rho^k \, dV$$
$$+ \int_{\mathscr{B}_0^e} \nabla N_\rho^i \cdot R_0 \nabla N_\rho^k \, dV$$

$$K_{IL}^{\rho\varphi} = \mathbf{A}_{e=1}^{n_{\text{el}}} - \int_{\mathscr{B}_0^e} N_\rho^i \partial_F \mathscr{R}_0 \cdot \nabla N_\varphi^l \, dV$$

$$\mathbf{K}_{JK}^{\varphi\rho} = \overset{n_{\text{el}}}{\underset{e=1}{\mathbf{A}}} \int\limits_{\mathscr{B}_0^e} \nabla N_\varphi^j \cdot \partial_{\rho_0} \bar{\mathbf{\Pi}}^t N_\rho^k \, dV$$

$$\mathbf{K}_{JL}^{\varphi\varphi} = \overset{n_{\text{el}}}{\underset{e=1}{\mathbf{A}}} \int\limits_{\mathscr{B}_0^e} N_\varphi^j \rho_0 \frac{1}{\Delta t^2} \mathbf{I} N_\varphi^l \, dV \tag{27}$$

$$+ \int\limits_{\mathscr{B}_0^e} \nabla N_\varphi^j \cdot \partial_F \bar{\mathbf{\Pi}}^t \cdot \nabla N_\varphi^l \, dV$$

Note, that the specification of the partial derivatives of the mass source $\mathscr{R}_0$ and the reduced momentum flux $\bar{\mathbf{\Pi}}^t$ with respect to the primary unknowns ρ_0 and φ depends on the particular choice of the constitutive equations. For the constitutive equations suggested in Sect. 3.3, we obtain the following expressions,

$$\partial_{\rho_0} \mathscr{R}_0 = c[n-m]\left[\frac{\rho_0}{\rho_0^*}\right]^{-m} \frac{1}{\rho_0} \Psi_0$$

$$\partial_F \mathscr{R}_0 = c\left[\frac{\rho_0}{\rho_0^*}\right]^{-m} \bar{\mathbf{\Pi}}^t$$

$$\partial_{\rho_0} \bar{\mathbf{\Pi}}^t = n\frac{1}{\rho_0} \bar{\mathbf{\Pi}}^t$$

$$\partial_F \bar{\mathbf{\Pi}}^t = \left[\frac{\rho_0}{\rho_0^*}\right]^n [\mu \mathbf{I}\bar{\otimes}\mathbf{I} + \lambda \mathbf{F}^{-t} \otimes \mathbf{F}^{-t} - [\lambda \ln J - \mu]\mathbf{F}^{-t}\underline{\otimes}\mathbf{F}^{-1}]$$

$$\tag{28}$$

whereby the component representations of the non-standard dyadic products read $\{\bullet\bar{\otimes}\circ\}_{ijkl} = \{\bullet\}_{ik} \otimes \{\circ\}_{jl}$ and $\{\bullet\underline{\otimes}\circ\}_{ijkl} = \{\bullet\}_{il} \otimes \{\circ\}_{jk}$. Finally, the solution of the system of equations (24) renders the iterative update for the increments of the global unknowns ρ_I and φ_J.

$$\Delta\rho_I = \Delta\rho_I + d\rho_I \quad \forall I = 1, \ldots, n_{n\rho}$$
$$\Delta\varphi_J = \Delta\varphi_J + d\varphi_J \quad \forall J = 1, \ldots, n_{n\varphi} \tag{29}$$

Remark 4.1 Within the node–based approach, we typically solve the balance of mass and momentum simultaneously on the global level assuming a $\mathscr{C}^0$–continuous interpolation of the density ρ_0 and the deformation φ. The only node-based finite element formulation that relaxes this continuity requirement is the Q1P0 element, which is based on an element-wise constant and thus $\mathscr{C}^{-1}$-continuous density interpolation. Recall, that for this element, which is classically applied for constrained problems arising in computational fluid dynamics or in incompressible elastodynamics, the constantly interpolated degree of freedom, in our case the density, can be eliminated locally on the element level. This procedure, which bares strong resemblance to the classical static condensation, results in the modified residual $\tilde{\mathbf{R}}_J^\varphi$ and the modified stiffness matrix $\tilde{\mathbf{K}}_{JL}^{\varphi\varphi}$.

$$\tilde{\mathbf{R}}_J^\varphi = \mathbf{R}_J^\varphi - \mathbf{K}_{JK}^{\varphi\rho}[K_{IK}^{\rho\rho}]^{-1}\mathbf{R}_I^\rho$$
$$\tilde{\mathbf{K}}_{JL}^{\varphi\varphi} = \mathbf{K}_{JL}^{\varphi\varphi} - \mathbf{K}_{JK}^{\varphi\rho}[K_{IK}^{\rho\rho}]^{-1}\mathbf{K}_{IL}^{\rho\varphi}$$

In the biomechanical literature, the algorithm resulting from an element-wise constant density distribution has been termed "element-based approach".

Remark 4.2 Within the biomechanical context, the evolution of the density ρ_0 and the deformation φ induces time scales which typically differ by orders of magnitude. To avoid the related numerical difficulties caused by the resulting ill–conditioned system matrices, the balance of momentum is usually evaluated in a quasi–static sense, i.e. the mechanical forces are interpreted as an average daily loading on the biological structure. Consequently, the first terms in the discrete momentum residual $N_\varphi^j \rho_0[\mathbf{p}_{0n+1} - \mathbf{p}_{0n}]\Delta t$ and in the tangent operator $N_\varphi^j \rho_0/\Delta t^2 \mathbf{I} N_\varphi^l$ in Eqs. (23)$_2$ and (27)$_4$ vanish identically.

Remark 4.3 When consistent dynamic matrices are applied to interpolate the time-dependent contributions, i.e. the $N_\rho^i[\rho_{0n+1} - \rho_{0n}]\Delta t$ and the $N_\rho^i 1/\Delta t N_\rho^k$ terms in Eqs. (23)$_1$ and (27)$_1$, the numerical solution might tend to develop spurious oscillations near sharp fronts. The use of lumped dynamic matrices typically reduces these numerical artifacts.

4.3
Algorithmic flowchart

A typical finite element-based solution algorithm resulting from the node-based approach is sketched in the flowchart in Table 1. It illustrates that the balance of mass and the balance of momentum are solved simultaneously on the global level.

Remark 4.4 It is worth noting that the numerical computation of the Q1P0 element with an elementwise constant density distribution requires some modifications in the algorithmic realization. In this particular case, the balance of mass and momentum are evaluated sequentially. First the midpoint density is advanced in time by performing a local Newton iteration on the element level. Only then, the balance of momentum is evaluated at each integration point with the element density given. Since the deformation φ_{n+1} is now the only unknown on the global level, the related residual and the tangential stiffness have to be modified according to Remark 4.1. Note, that within the Q1P0 approach the evolution of the element density is driven by the average element mass source.

$$\frac{\rho_{0n+1} - \rho_{0n}}{\Delta t} = \frac{1}{V} \int\limits_{\mathscr{B}_0^e} \mathscr{R}_0(\rho_{0n+1}, \varphi_{n+1}) dV$$

Table 1. Algorithm of node-based approach

loop over all time steps
global Newton iteration
loop over all elements
loop over all integration points
evaluate balance of mass and momentum
determine $R^{\rho e}$, $\mathbf{R}^{\varphi e}$, $\partial_\rho R^{\rho e}$, $\partial_\varphi R^{\rho e}$, $\partial_\rho \mathbf{R}^{\varphi e}$, $\partial_\varphi \mathbf{R}^{\varphi e}$
element residuals and their partial derivatives
determine R^ρ, $\mathbf{R}^\varphi$, $K^{\rho\rho}$, $\mathbf{K}^{\rho\varphi}$, $\mathbf{K}^{\varphi\rho}$, $\mathbf{K}^{\varphi\varphi}$
global residuals and iteration matrices
determine ρ_{n+1} and φ_{n+1}
determine state of biological equilibrium

Since the driving force $\mathscr{R}_0$ is a nonlinear function of the deformation φ_{n+1}, it has to be evaluated numerically by an appropriate numerical integration before the element density can be determined through the suggested local Newton iteration.

4.4
Illustration in terms of model problem
To illustrate the features of the node-based approach, we shall now elaborate its behavior with respect to two academic model problems upon which the first relates to a discontinuous solution whereas the solution of the second is supposed to be continuous. These two examples somehow represent the extreme cases we assume to encounter in realistic biomechanical applications. In both cases, we analyze a similar tension specimen of unit length with a length to width ratio of 1%. The elastic material parameters are chosen to $E = 1$ and $v = 0.2$, which correspond to $\lambda = 0.2778$ and $\mu = 0.4167$. The growth–related parameters take values of $\rho_0^* = 1$, $\Psi_0^* = 2$, $c = 1$, $n = 2$ and $m = 3$, whereby stability is guaranteed as $m > n$. A unit tensile load is applied to both ends of the specimen. In combination with the chosen set of parameters, this load generates stretches of about 250%. To guarantee convergence within the global Newton iteration, the load has to be applied incrementally in ten steps of 0.1 each. After the loading phase, the load is held constant for another 50 time steps of $\Delta t = 0.1$ while the solution converges towards the biological equilibrium state.

Figure 1 depicts the four applied finite element formulations as typical representatives of the node–based approach, whereby the white circles characterize the density nodes whereas the dark circles mark the deformation nodes. While the classical Q1Q1 and Q2Q2 element are based on an equal order interpolation of the density and the deformation field, the Q1P0 element and the S2Q1 element interpolate the density one order lower than the deformation. All elements except for the Q2Q2 element which is evaluated numerically at 3×3 integration points make use of a Gauss–Legendre quadrature based on 2×2 integration points.

The resulting number of degrees of freedom and the number of integration points as characteristic measures of computational efficiency are given in Table 2. Thereby, the individual columns are related to a discretization with 10,
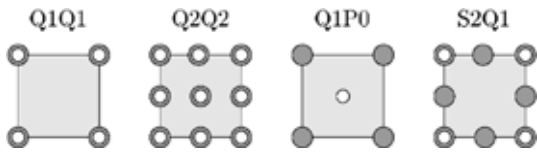

Fig. 1. Different finite elements – node-based approach

Table 2. Degrees of freedom and integration points

	$n_{\text{el}} = 10$	$n_{\text{el}} = 40$	$n_{\text{el}} = 100$
Q1Q1	$66^{(40)}$	$246^{(160)}$	$606^{(400)}$
Q2Q2	$189^{(90)}$	$729^{(360)}$	$1809^{(900)}$
Q1P0	$44^{(90)}$	$164^{(360)}$	$404^{(900)}$
S2Q1	$128^{(40)}$	$488^{(160)}$	$1208^{(400)}$

40 and 100 elements, thus representing a typical h-refinement. The rows which correspond to the different element formulations can be interpreted as a sort of p-refinement.

4.4.1
Discontinuous model problem
First, we trigger a discontinuous solution by varying the value of the attractor stimulus Ψ_0^* from $\Psi_0^* = 2.0$ at both ends in discrete steps of $\Delta\Psi_0^* = -0.25$ towards $\Psi_0^* = 1.0$ in the middle of the specimen. Obviously, the local reduction of the attractor stimulus has a direct influence on the creation of new material. The decrease of its value is compensated by a considerable local increase in density, as illustrated in Fig. 2. The quantitative results of the discontinuous model problem are summarized in Tables 3 and 4, which show the relative change in density $[\rho_0 - \rho_0^*]/\rho_0^*$ in the center of the specimen and the end-point displacement u, respectively. The depicted density distributions illustrate that the Q1Q1 element produces spurious oscillations close to sharp fronts. It converges to the discontinuous solution upon mesh refinement, however, the artificial overshoots in the solution remain. The element of highest order, the Q2Q2 element, performs worst upon all elements, compare also Tables 3 and 4. The corresponding density distribution is too smooth by far and the results are only valuable upon a considerable mesh refinement. Since the Q2Q2 element is the most expensive element from a computational point of view, it can be classified as non-reasonable for practical use. For this particular discontinuous type of solution, the Q1P0 element with a $\mathscr{C}^{-1}$-continuous density interpolation performs best upon all elements tested. With an elementwise constant density distribution, it is able to capture sharp fronts by construction. The S2Q1 element shows a less oscillatory behavior than the Q1Q1 element. Unlike the Q2Q2 element, it is able to capture discontinuities in a reasonable way. It converges fast upon refinement and is also not too expensive from a computational point of view.

4.4.2
Continuous model problem
The second example is based upon a continuous solution which is generated by smoothly varying the width of the specimen from 1% of the specimen length at both ends towards 0.5% in the middle of the bar. Thereby, the material parameters are kept constant throughout the specimen. The characteristics of the different elements for a continuous solution can be concluded from Fig. 3 and Tables 5 and 6. Obviously, the local reduction of the cross section is directly compensated by the creation of material in the center of the specimen. Remarkably, all node-based formulations of a $\mathscr{C}^0$-continuous density interpolation perform equally well for this sufficiently smooth problem. Already for the discretization with 40 elements, the results of the Q1Q1 element, the Q2Q2 element and the S2Q1 element have converged to a reasonable extend, since their continuous density interpolations are typically designed to capture continuous solutions. While the Q1P0 element yields useless results for the coarsest mesh, it converges rapidly upon mesh refinement
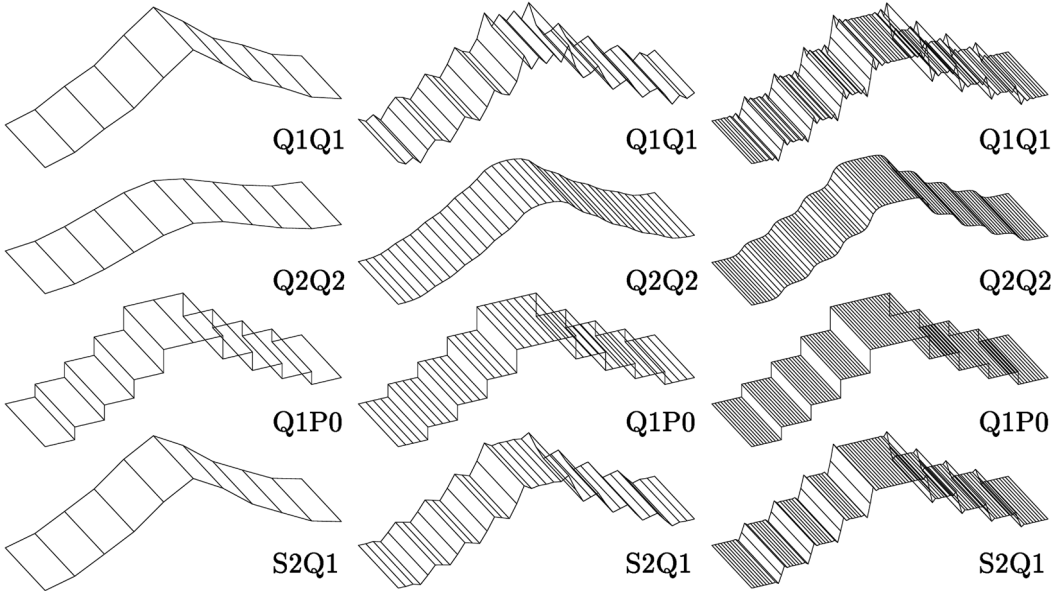
Fig. 2. Discontinuous model problem – density distribution of node–based approach – Q1Q1, Q2Q2, Q1P0 and S2Q1 elements

Table 3. Discontinuous model problem – relative change in density $[\rho_0 - \rho_0^*]/\rho_0^*$ at midpoint

	$n_{\mathrm{el}} = 10$	$n_{\mathrm{el}} = 40$	$n_{\mathrm{el}} = 100$
Q1Q1	0.321502	0.297437	0.305828
Q2Q2	0.256541	0.302062	0.306116
Q1P0	0.300028	0.306185	0.306171
S2Q1	0.318560	0.305875	0.306171

Table 4. Discontinuous model problem – endpoint displacement u

	$n_{\mathrm{el}} = 10$	$n_{\mathrm{el}} = 40$	$n_{\mathrm{el}} = 100$
Q1Q1	2.32251	2.37135	2.36629
Q2Q2	2.37124	2.37151	2.37156
Q1P0	2.32239	2.37122	2.36624
S2Q1	2.37221	2.37181	2.37166

even though it applies only a $\mathscr{C}^{-1}$-continuous density interpolation, see also Tables 5 and 6.

5
Integration point–based approach
In contrast to the previous approach, we shall now relax the assumption of $\mathscr{C}^0$ continuity for the density field ρ_0 and allow for a discrete pointwise density representation while the deformation field φ is, of course, still required to be $\mathscr{C}^0$-continuous. Consequently, the balance of mass can be evaluated locally on the integration point level, whereas the global system of equations is expressed in terms of the deformation only. By introducing the density as internal variable on the integration point level, we solve the balance of mass and momentum in a staggered sense. Recall, that by
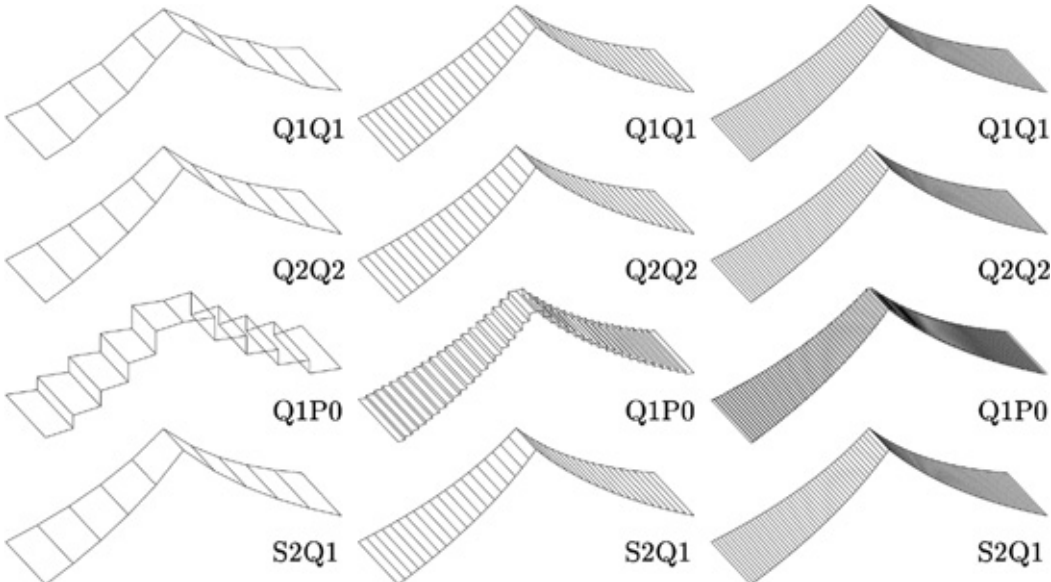

Fig. 3. Continuous model problem – density distribution of node-based approach – Q1Q1, Q2Q2, Q1P0 and S2Q1 elements

Table 5. Continuous model problem – relative change in density $[\rho_0 - \rho_0^*]/\rho_0^*$ at midpoint

	$n_{el} = 10$	$n_{el} = 40$	$n_{el} = 100$
Q1Q1	0.509938	0.525144	0.527496
Q2Q2	0.527441	0.527699	0.534161
Q1P0	0.470753	0.513734	0.522864
S2Q1	0.526425	0.528890	0.529023

Table 6. Continuous model problem – endpoint displacement u

	$n_{el} = 10$	$n_{el} = 40$	$n_{el} = 100$
Q1Q1	2.92605	2.92755	2.92780
Q2Q2	2.92732	2.92785	2.92793
Q1P0	2.92554	2.92752	2.92780
S2Q1	2.92792	2.92794	2.92794

relaxing the continuity requirement for the density, we a priori exclude the possibility of incorporating a mass flux.

5.1
Spatial discretization
In complete analogy to the previous section, the spatial discretization is based on the partition of the domain of interest $\mathscr{B}_0$ into n_{el} elements $\mathscr{B}_0^e$

$$\mathscr{B}_0 = \bigcup_{e=1}^{n_{el}} \mathscr{B}_0^e \tag{30}$$

on which the element geometry $\mathbf{X}^h$ is interpolated as $\mathbf{X}^h|_{\mathscr{B}_0^e} = \sum_{i=1}^{n_{eX}} N_X^i \mathbf{X}_i$. According to the isoparametric concept in combination with the Bubnov–Galerkin technique, similar basis functions N are applied for the interpolation of the test and trial functions $\delta\boldsymbol{\varphi}^h$ and $\boldsymbol{\varphi}^h$.

$$\delta\boldsymbol{\varphi}^h|_{\mathscr{B}_0^e} = \sum_{j=1}^{n_{e\varphi}} N_\varphi^j \delta\boldsymbol{\varphi}_j \in H_1^0(\mathscr{B}_0)$$
$$\boldsymbol{\varphi}^h|_{\mathscr{B}_0^e} = \sum_{l=1}^{n_{e\varphi}} N_\varphi^l \boldsymbol{\varphi}_l \in H_1(\mathscr{B}_0) \tag{31}$$

Consequently, the spatial gradients of the test and trial functions $\nabla\delta\boldsymbol{\varphi}^h$ and $\nabla\boldsymbol{\varphi}^h$ can be expressed in the following form.

$$\nabla\delta\boldsymbol{\varphi}^h|_{\mathscr{B}_0^e} = \sum_{j=1}^{n_{e\varphi}} \delta\boldsymbol{\varphi}_j \otimes \nabla N_\varphi^j$$
$$\nabla\boldsymbol{\varphi}^h|_{\mathscr{B}_0^e} = \sum_{l=1}^{n_{e\varphi}} \boldsymbol{\varphi}_l \otimes \nabla N_\varphi^l \tag{32}$$

The algorithmic balance of momentum can thus be stated as

$$\mathbf{R}_J^\varphi(\boldsymbol{\varphi}_{n+1}^h) = \mathbf{0} \quad \forall J = 1, \ldots, n_\varphi \tag{33}$$

whereby the discrete residual $\mathbf{R}_J^\varphi$ is defined in the following form.

$$\mathbf{R}_J^\varphi = \mathop{\mathbf{A}}_{e=1}^{n_{el}} \int_{\mathscr{B}_0^e} N_\varphi^j \rho_0 \frac{\mathbf{p}_{n+1} - \mathbf{p}_n}{\Delta t} + \nabla N_\varphi^j \cdot \bar{\boldsymbol{\Pi}}_{n+1} \, dV$$
$$- \int_{\partial\mathscr{B}_0^{te}} N_\varphi^j [\mathbf{t}_{n+1}^{closed} + \bar{\mathbf{t}}_{n+1}^{open}] dA - \int_{\mathscr{B}_0^e} N_\varphi^j \bar{\mathbf{b}}_{0n+1} dV \tag{34}$$

5.2
Linearization
Similar to the previous chapter, the nonlinear equilibrium equation (33) is solved within the incremental iterative Newton–Raphson iteration scheme requiring a consistent linearization at time t_{n+1}.

$$\mathbf{R}_{J\,n+1}^{\varphi k+1} = \mathbf{R}_{J\,n+1}^{\varphi k} + d\mathbf{R}_J^\varphi \doteq \mathbf{0} \quad \forall J = 1, \ldots, n_{n\varphi} \tag{35}$$

The iterative residual $d\mathbf{R}_J^\varphi$

$$d\mathbf{R}_J^\varphi = \sum_{L=1}^{n_{n\varphi}} \mathbf{K}_{JL}^{\varphi\varphi} \cdot d\boldsymbol{\varphi}_L \tag{36}$$

can be expressed in terms of the iteration matrix

$$\mathbf{K}_{JL}^{\varphi\varphi} = \frac{\partial \mathbf{R}_J^\varphi}{\partial \boldsymbol{\varphi}_L} \tag{37}$$

which takes the interpretation of the global tangential stiffness matrix.

$$\mathbf{K}_{JL}^{\varphi\varphi} = \mathop{\mathbf{A}}_{e=1}^{n_{el}} \int_{\mathscr{B}_0} N^j \rho_0 \frac{1}{\Delta t} \mathbf{I} N^l \, dV + \int_{\mathscr{B}_0} \nabla N^j \cdot d_F \bar{\boldsymbol{\Pi}}^t \cdot \nabla N^l \, dV \tag{38}$$

Therein, $d_F \bar{\boldsymbol{\Pi}}^t$ denotes the consistent tangent operator

$$d_F \bar{\boldsymbol{\Pi}}^t = \partial_F \bar{\boldsymbol{\Pi}}^t - \partial_{\rho_0} \bar{\boldsymbol{\Pi}}^t \left[\overline{\partial_{\rho_0} \mathscr{R}_0} \right]^{-1} \partial_F \mathscr{R}_0 \tag{39}$$

whereby $\partial_F \bar{\boldsymbol{\Pi}}^t$, $\partial_{\rho_0} \bar{\boldsymbol{\Pi}}^t$ and $\partial_F \mathscr{R}_0$ were already given in Eq. (28), while $\overline{\partial_{\rho_0} \mathscr{R}_0}$ can be expressed in the following form.

$$\overline{\partial_{\rho_0} \mathscr{R}_0} = c[n - m] \frac{1}{\rho_0} \left[\frac{\rho_0}{\rho_0^*} \right]^{-m} \Psi_0 \Delta t - 1 \tag{40}$$

The iterative update for the incrementals of the global unknowns $\boldsymbol{\varphi}_J$

$$\Delta\boldsymbol{\varphi}_J = \Delta\boldsymbol{\varphi}_J + d\boldsymbol{\varphi}_J \quad \forall J = 1, \ldots, n_{n\varphi} \tag{41}$$

can finally be determined in terms of the solution $d\boldsymbol{\varphi}_J$ of the linearized system of equations (35).
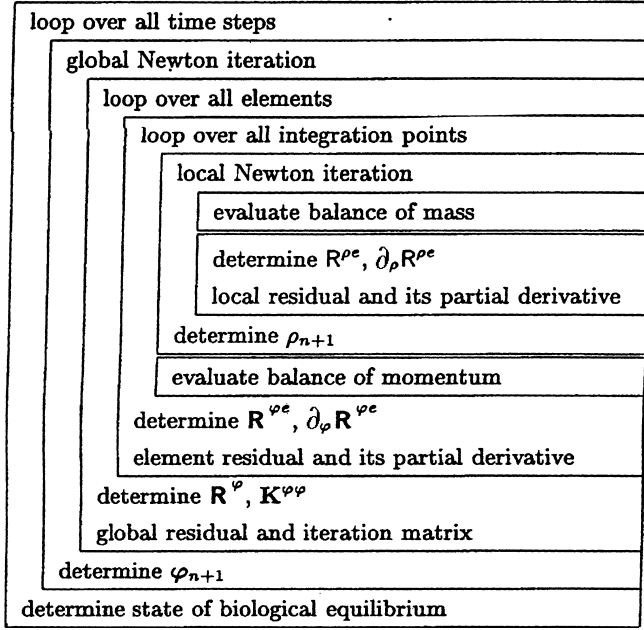
Remark 5.1 Note, that the structure of the consistent tangent operator introduced in Eq. (39) resembles the structure of the modified element stiffness matrix after static condensation defined in Remark 4.1.

$$d_F \bar{\boldsymbol{\Pi}}^t = \partial_F \bar{\boldsymbol{\Pi}}^t - \partial_{\rho_0} \bar{\boldsymbol{\Pi}}^t \left[\overline{\partial_{\rho_0} \mathscr{R}_0} \right]^{-1} \partial_F \mathscr{R}_0$$
$$\tilde{\mathbf{K}}_{JL}^{\varphi\varphi} = \mathbf{K}_{JL}^{\varphi\varphi} - \mathbf{K}_{JK}^{\varphi\rho} [K_{IK}^{\rho\rho}]^{-1} \mathbf{K}_{IL}^{\rho\varphi}$$

The difference between the terms $\overline{\partial_{\rho_0} \mathscr{R}_0}$ and $\partial_{\rho_0} \mathscr{R}_0$ somehow reflects the influence of the algorithmic

Table 7. Algorithm of integration point-based approach

```
loop over all time steps
  global Newton iteration
    loop over all elements
      loop over all integration points
        local Newton iteration
          evaluate balance of mass
          determine Rᵖᵉ, ∂_ρRᵖᵉ
          local residual and its partial derivative
        determine ρₙ₊₁
      evaluate balance of momentum
      determine R^φe, ∂_φR^φe
      element residual and its partial derivative
    determine R^φ, K^φφ
    global residual and iteration matrix
  determine φₙ₊₁
determine state of biological equilibrium
```


Fig. 4. Different elements – integration point-based approach

Table 8. Degrees of freedom and integration points

	$n_{el} = 10$	$n_{el} = 40$	$n_{el} = 100$
Q1	$44^{(40)}$	$164^{(160)}$	$404^{(400)}$
Q2	$126^{(90)}$	$486^{(360)}$	$1206^{(900)}$
Q1^{sri}	$44^{(10/40)}$	$164^{(40/160)}$	$404^{(100/400)}$
S2^{fri}	$106^{(40)}$	$406^{(160)}$	$1006^{(400)}$

treatment. By replacing the continuous term $\partial_{\rho_0}\mathscr{R}_0$ with its algorithmic counterpart $\overline{\partial_{\rho_0}\mathscr{R}_0}$ we ensure the consistent linearization of the discrete constitutive equations.

5.3
Algorithmic flowchart
Table 7 illustrates a typical flowchart resulting from the integration point-based approach. The balance equations are solved in a staggered way, characterized through a local Newton iteration for the actual integration point density embedded in the global Newton iteration for the deformation field.

Remark 5.2 Similar to the node-based approach, the realization of an elementwise constant density distribution based on a selective reduced integration of the scalar field requires some algorithmic modifications. In this case, the balance of mass and momentum are solved sequentially. Just like for the Q1P0 element, the actual midpoint density has to be determined in a local Newton iteration before the balance of momentum is evaluated on the integration point level. In contrast to the Q1P0 element, however, the density evolution is now driven by the midpoint mass source.

$$\frac{\rho_{0n+1} - \rho_{0n}}{\Delta t} = \mathscr{R}_0\big(\rho_{0n+1}, \boldsymbol{\varphi}_{n+1}\big)\big|_{\xi=0}$$

As the mass source $\mathscr{R}_0$ is a nonlinear function of the deformation $\boldsymbol{\varphi}_{n+1}$, its midpoint value generally differs from its element average. Consequently, the Q1P0 element and the Q1^{sri} element generally render different results. The significance of this difference strongly depends on the inhomogeneity of the discrete deformation field $\boldsymbol{\varphi}_{n+1}$ and vanishes identically for a homogeneous deformation.

5.4
Illustration in terms of model problem
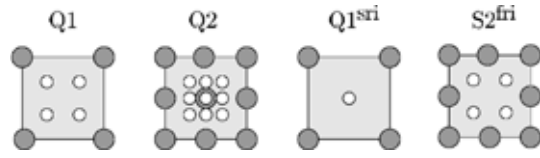We now turn to the illustration of the integration point–based approach in terms of the discontinuous and the continuous model problem defined in chapter 4. The analyzed element formulations are depicted in Fig. 4.

While the Q1 and the Q2 element are classically integrated with 2×2 and 3×3 quadrature points, respectively, the Q1^{sri} element is based on a selective reduced one–point–integration of the density part in combination with a 2×2 integration of the deformation part. The S2^{fri} element, however, applies a fully reduced 2×2 integration of both contributions.

The number of degrees of freedom and integration points, which is considerably lower than in the previous node-based approach, is depicted in Table 8.

5.4.1
Discontinuous model problem
The resulting density distribution, the relative change in density $[\rho_0 - \rho_0^*]/\rho_0^*$ in the middle of the specimen and the endpoint displacement u are given in Fig. 5 and Tables 9 and 10, respectively. Note, that in order to illustrate the typical features of the integration point–based approach, the integration point values are plotted in a non-smoothed discontinuous fashion. Unlike in classical finite element post–processing, where the integration point values are typically extrapolated to the nodes and then averaged, we plot the actual constant integration point value in the entire area that is assigned to the particular quadrature point. As expected, all elements with the density as internal variable perform excellent for this particular discontinuous problem. By construction, the integration point–based approach is ideally suited for discontinuous solutions with sharp fronts.

5.4.2
Continuous model problem
Even for the continuous problem, the integration point–based elements perform remarkably well. Not only the classical Q1 element and the Q2 element but also the Q1^{sri} element and the S2^{fri} element converge fast upon mesh refinement, compare also Fig. 6 and Tables 11 and 12. Thereby, the computationally cheapest approaches, namely the Q1 element and the selective reduced integrated Q1^{sri} element show only minor differences. Both of them can thus be classified as extremely fast and efficient
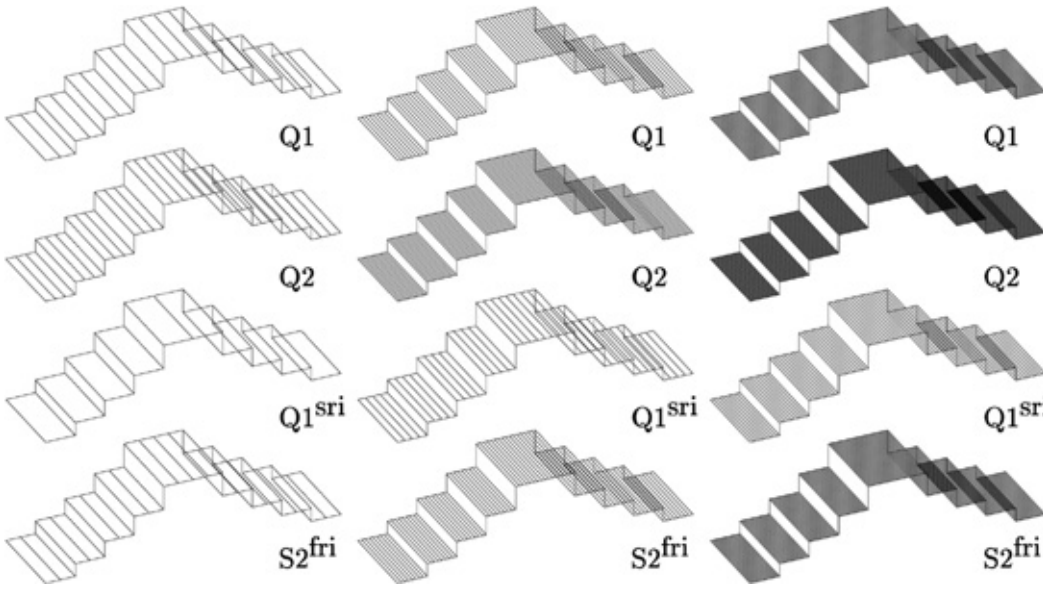
Fig. 5. Discontinuous model problem – density distribution of integration point-based approach – Q1, Q2, Q1$^{\text{sri}}$ and S2$^{\text{fri}}$ elements

Table 9. Discontinuous model problem – relative change in density $[\rho_0 - \rho_0^*]/\rho_0^*$ at midpoint

	$n_{\text{el}} = 10$	$n_{\text{el}} = 40$	$n_{\text{el}} = 100$
Q1	0.300028	0.306185	0.306418
Q2	0.306443	0.306186	0.306188
Q1$^{\text{sri}}$	0.300028	0.306168	0.306171
S2$^{\text{fri}}$	0.306504	0.306282	0.306171

Table 10. Discontinuous model problem – endpoint displacement u

	$n_{\text{el}} = 10$	$n_{\text{el}} = 40$	$n_{\text{el}} = 100$
Q1	2.32239	2.37122	2.36624
Q2	2.37095	2.37146	2.37154
Q1$^{\text{sri}}$	2.32239	2.37135	2.36630
S2$^{\text{fri}}$	2.37156	2.37155	2.37155

for practical use. Nevertheless, due to the standard computational structure of the related numerical algorithm, we prefer the classical Q1 element over the Q1$^{\text{sri}}$ element for practical applications.

Remark 5.3 This particular model problem still shows a rather homogeneous deformation in each element. Thus, the difference between the Q1P0 element and the Q1$^{\text{sri}}$ element is only of minor nature. However, by comparing the resulting maximum density and the endpoint displacements, slight deviations of both approaches can be detected.

6
Representative example
Finally, the derived classes of algorithms shall be compared in terms of a representative example from biome-
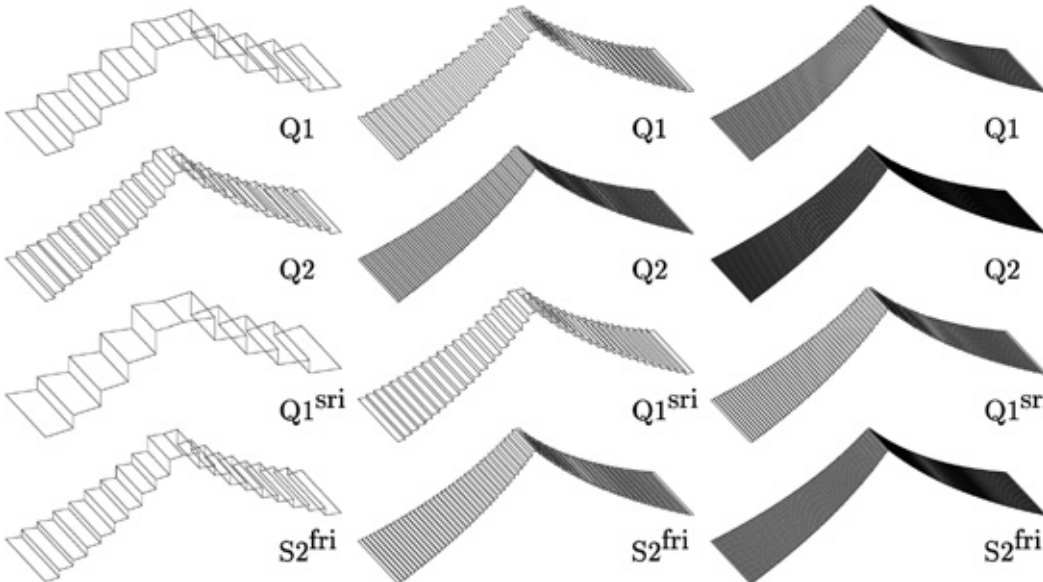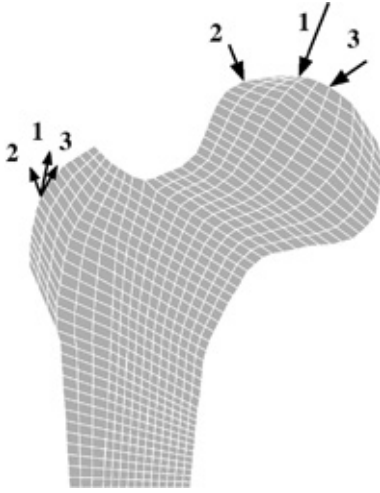

Fig. 6. Continuous model problem – density distribution of integration point-based approach – Q1, Q2, Q1$^{\text{sri}}$ and S2$^{\text{fri}}$ elements

Table 11. Continuous model problem – relative change in density $[\rho_0 - \rho_0^*]/\rho_0^*$ at midpoint

	$n_{\text{el}} = 10$	$n_{\text{el}} = 40$	$n_{\text{el}} = 100$
Q1	0.470754	0.513734	0.522864
Q2	0.514584	0.526201	0.529164
Q1$^{\text{sri}}$	0.470753	0.513734	0.522864
S2$^{\text{fri}}$	0.503670	0.522526	0.526427

Table 12. Continuous model problem – endpoint displacement u

	$n_{\text{el}} = 10$	$n_{\text{el}} = 40$	$n_{\text{el}} = 100$
Q1	2.92548	2.92751	2.92780
Q2	2.92732	2.92785	2.92793
Q1$^{\text{sri}}$	2.92599	2.92765	2.92786
S2$^{\text{fri}}$	2.92789	2.92794	2.92794

Fig. 7. Proxima femur – loading conditions

Table 13. Proxima femur – loading conditions

Load case	Value (N)	Direction (°)	Value (N)	Direction (°)
1	2317	24	703	28
2	1158	−15	351	−8
3	1548	56	468	35

Table 14. Number of elements, degrees of freedom and integration points

	n_{el}	n_{dof}	n_{ip}
Q1Q1	658	2175	2632
Q1Q1	2632	8295	10528
Q1Q1	5922	18363	23688
Q2Q2	658	8295	5922
Q1P0	658	1450	2632
S2Q1	658	4939	2632
Q1	658	1450	2632
Q2	658	5530	5922
Q1$^{\text{sri}}$	658	1450	658/2632
S2$^{\text{fri}}$	658	4214	2632

chanics. To this end, we study the classical benchmark problem of bone remodeling of the proxima femur subjected to an average daily loading situation. A detailed specification of the problem is given by Carter and Beaupré [2]. For the model suggested herein, we chose the elastic parameters to $E = 500$ and $v = 0.2$ corresponding to $\lambda = 138,8889$ and $\mu = 208,3333$. while the additional growth-related parameters are chosen to $\rho_0^* = 1.2$, $\Psi_0^* = 0.01$, $c = 1$, $n = 2$ and $m = 3$. The geometry and the loading conditions are depicted in Fig. 7. Typically, three different loading situations can be identified. Load case 1 corresponds to the load condition for the midstance phase of gait, while load cases 2 and 3 represent the extreme cases of abduction and adduction defined in Table 13.

The different elements and the corresponding number of degrees of freedom and integration points as a typical measure for the computational efficiency is given in Table 14. Figures 8–11 illustrate the distribution of the relative changes in density $[\rho_0 - \rho_0^*]/\rho_0^*$ as a result of the different spatial discretization techniques. The first set of

Fig. 8 illustrates the behavior of the Q1Q1 element with respect to h-refinement. The results do not differ considerably upon refinement of the mesh. Remarkably, already the coarsest mesh with 658 elements seems to be sufficient to capture the typical biomechanical characteristics of the solution: the development of a dense system of compressive trabeculae carrying the stress from the superior contact surface to the calcar region of the medial cortex, a secondary arc system of trabeculae through the inferomedial joint surface into the lateral metaphyseal region, the formation of Ward's triangle and the development of a dense cortical shaft around the medullary core. Consequently, we shall restrict our further analyses to the coarsest 658-element mesh.

Figure 9 contrasts the results of the different node-based finite element formulations. Remarkably, the Q1Q1 element, the Q2Q2 element, the Q1P0 element and the S2Q1 element render nearly identical results. Unlike reported in the related literature, the Q1P0 formulation with an elementwise constant density interpolation does not show any spatial instabilities. Due to the choice of a well–posed continuum formulation in combination with an implicit time integration scheme, all finite element formulations, even the one based on an elementwise constant density interpolation, render stable and unique results.

Figures 10 and 11 show the integration point-based counterpart of the solution which result from the classical Q1 element, the Q2 element, the selectively reduced integrated Q1$^{\text{sri}}$ element and the fully reduced integrated S2$^{\text{fri}}$ element. While Fig. 10 depicts the discrete values of the internal variables for each area assigned to the corresponding quadrature point, Fig. 11 illustrates the classical post-processing result that is obtained by an extrapolation of the integration point values to the nodes in combination with an averaging of these nodal values. The Q1 element and the S2$^{\text{fri}}$ element apply the same number of integration points per element. However, the
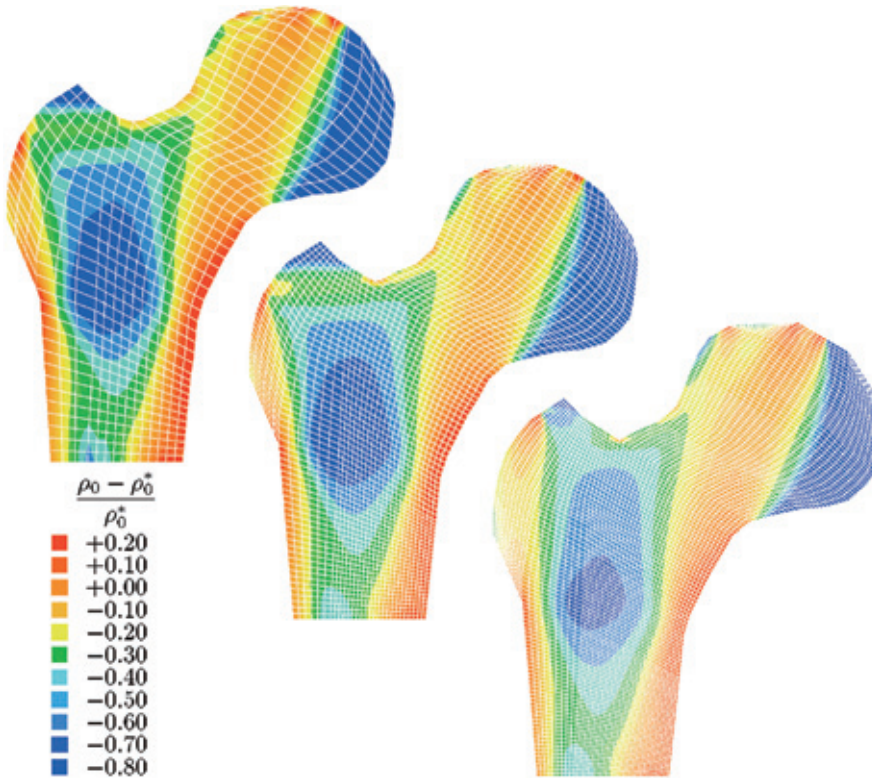
Fig. 8. Proxima femur – density distribution of node-based approach – 658, 2632 and 5922 Q1Q1 elements
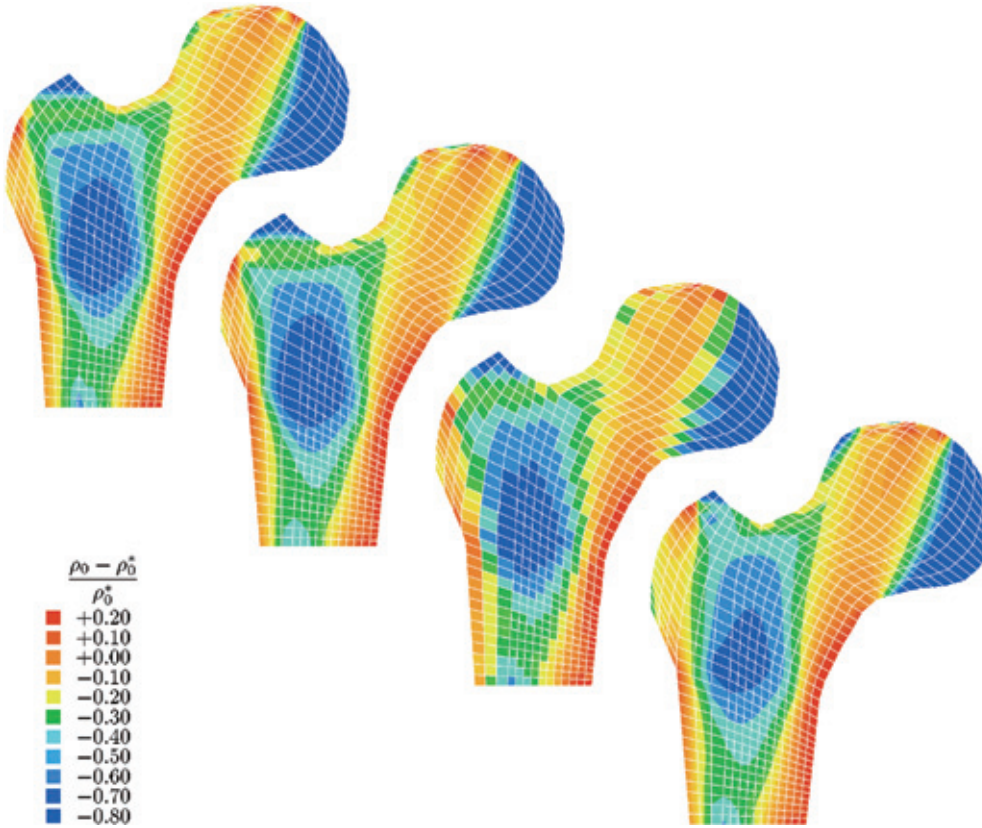

Fig. 9. Proxima femur – density distribution of node-based approach – 658 Q1Q1, Q2Q2, Q1P0 and S2Q1 elements

solution of the classical Q1 element seems to be slightly oscillatory while the S2^{fri} solution is rather smooth due to its quadratic interpolation of the deformation field. Since the solution is rather homogeneous within each element, the integration point-based Q1^{sri} element renders nearly identical results as the node-based Q1P0 element. The differences of the individual integration point-based elements vanish upon smoothing as illustrated in Fig. 11.
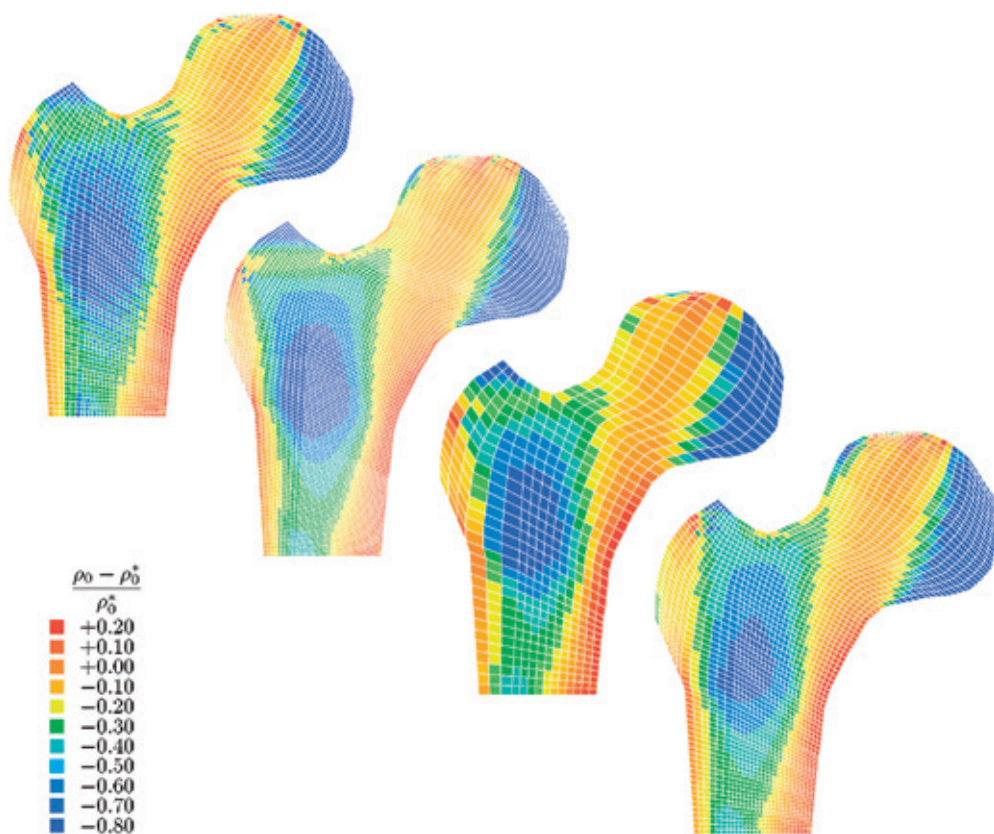
Fig. 10. Proxima femur – density distribution of integration point-based approach – 658 Q1, Q2, Q1^{sri} and S2^{fri} elements
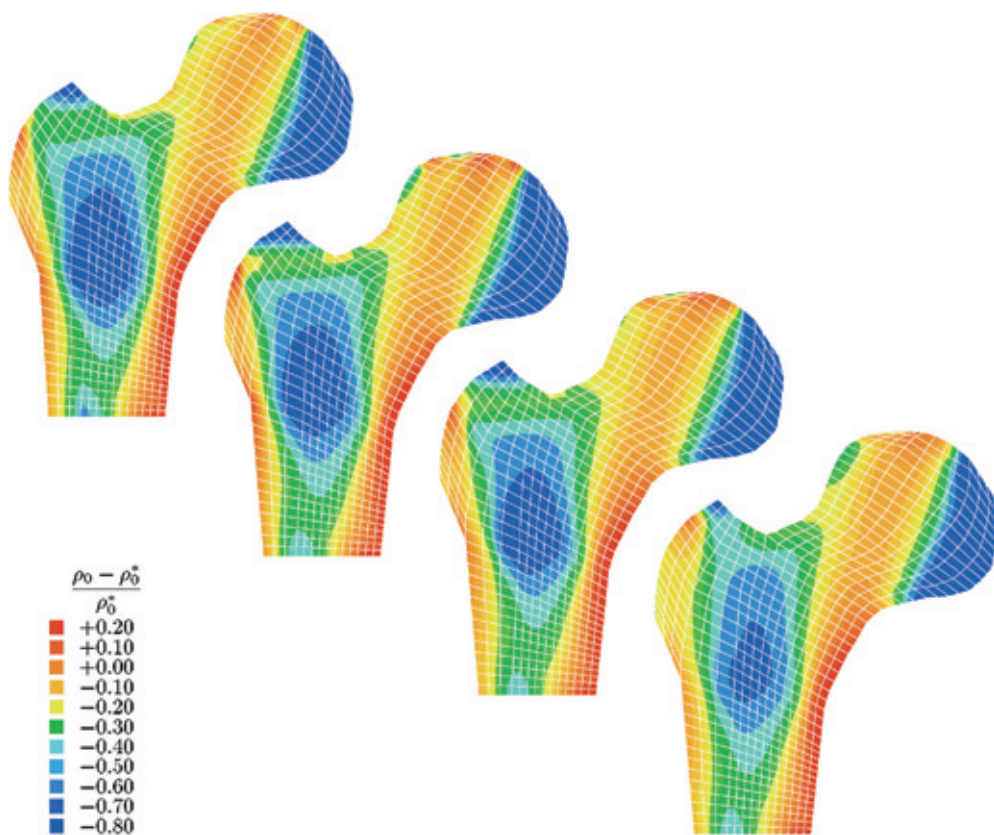

Fig. 11. Proxima femur – density distribution integration point-based approach – 658 Q1, Q2, Q1^{sri} and S2^{fri} elements-smoothed

By making use of the traditional post-processing step as typically applied for the graphic representation of internal variables, all results of the integration point-based approach are nearly alike. Moreover, they all roughly correspond to the results of the node-based approach depicted in Fig. 9.
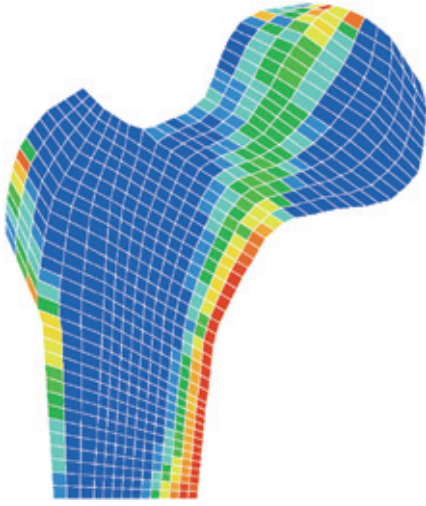
Fig. 12. Proxima femur – density distribution of node-based approach – Q1P0 element – unstable continuum model with $n = 2$ and $m = 0$

Remark 6.1 Within the present approach, neither the node-based Q1P0 element nor the integration point-based Q1^{sri} element tend to develop the spatial instabilities reported in the literature. To document the fact, that these spatial instabilities are already introduced on the continuum level and then, of course, carry over to the temporally and spatially discrete problem, we analyzed the similar problem described above, only now with the parameters $n = 2$ and $m = 0$. According to Harrigan and Hamilton [17, 19], this set of parameters is supposed to produce a non-unique and unstable solution. The numerical result depicted in Fig. 12 shows the typical discontinuous 0–1 type of solution with the classical tendency towards checker-boarding. The given density distribution corresponds to the last converged state within the simulation; the calculation stopped after half of the prescribed time period because of the loss of convergence within the global Newton iteration caused by ill-conditioned system matrices.

7
Discussion
The basic concern of the present work was the comparison of different computational strategies to model growth processes typically encountered in modern biomechanical applications. Motivated by the huge body of literature on this highly active branch of research, we began by comparing the existing formulations in terms of appropriated classifications. It turned out, that the notions of stability and uniqueness were often attributed to the temporal or to the spatial discretization although the cause of instability actually originated back to the ill-posedness of the underlying continuous problem. We thus presented a well-posed continuum model embedded in the framework of finite deformations. Unlike the existing small strain formulations, the derived geometrically exact model is not a priori restricted to hard tissue mechanics but is potentially able to simulate the behavior of soft tissues. In contrast to most existing formulations in the literature, we suggested

the use of an implicit time stepping scheme which is unconditionally stable and thus poses no additional restrictions on the choice of the time step size.

The analysis of different spatial discretization techniques constituted the main part of this contribution. While the deformation field is treated in the classical way, we suggested two alternative discretization strategies for the density field, a node-based and an integration point-based approach. For the former, the density is introduced as a global unknown on the nodal level, whereas it is treated as an internal variable on the integration point level in the latter approach. The traditional element-based approach can then be classified as a special case of either the node-based or the integration point-based approach. For the geometrically exact formulation analyzed herein, the corresponding finite element formulations, namely the Q1P0 element and the Q1^{sri} element, showed a slightly different behavior, while for the linear elastic model applied in the literature, both formulations should be absolutely identical. In the context of modern finite element technologies, the discretized equations were linearized consistently and their solution was embedded in an incremental iterative Newton-Raphson procedure.

Both alternative discretization strategies were finally compared numerically in terms of a discontinuous and a continuous model problem and the classical application of bone remodeling in the proxima femur. As expected, the node-based elements performed better for continuous smooth solutions while the integration point-based elements proved advantageous for discontinuous problems with sharp fronts. Despite of this difference, both strategies yielded remarkably similar results upon mesh refinement. In most of the cases, the analyzed lower order elements, i.e. the Q1P0 element, the classical Q1 element and the Q1^{sri} element, were superior over the higher order elements. They proved computationally cheap, i.e. cheap in memory, storage and computer time, and thus turned out to be extremely fast. Especially the computationally most expensive Q2Q2 element performed poor close to sharp fronts and is thus not recommended for further practical use.

Another remarkable difference between the two alternative discretization techniques is the size of the overall problem, which is directly related to the computer time required for the solution. For small scale problems, both strategies needed approximately the same calculation time. While the node-based approach basically suffers from larger system matrices, the integration point-based approach requires a local Newton iteration at the integration point level. Nevertheless, the influence of the former becomes more and more pronounced upon mesh refinement. Provided that both strategies give similar results, this lack of computational efficiency of the node-based approach might be an important drawback for realistic large scale simulations. However, one has to keep in mind, that the node-based approach becomes unavoidable, if higher order gradients of the density are to be incorporated, e.g. by the incorporation of a mass flux or by the need to reproduce the classical size effect.

Finally, we would like to conclude by pointing out, that the results of the present study are not necessarily

restricted to the modeling of growth but rather hold in a more general sense. Any multi-field problem in continuum mechanics, e.g. convection–diffusion in chemo-mechanical applications, the classical thermo-elasticity or problems arising in inelasticity such as damage or plasticity, can be treated in an analogous way. As long as no gradients of the additional field, e.g. the concentration, the temperature, the damage variable or the plastic multiplier, are incorporated in the formulation, one is free to choose either a $\mathscr{C}^0$-continuous node-based approach or a discrete pointwise representation within the integration point-based approach. Upon mesh refinement, both strategies should converge to the same solution, provided that the different interpolation orders of the individual fields are chosen appropriately. As soon as higher order spatial gradients enter the formulation, e.g. through diffusion, heat conduction, gradient damage or gradient plasticity, the node-based $\mathscr{C}^0$-continuous approach becomes mandatory. In this sense, the present work is believed not only to yield a contribution to the computational modeling of growth in particular but also to the numerical simulation of multi-field problems in general.

References

1. Beaupré GS, Orr TE, Carter DR (1990) An approach for time–dependent bone modelling and remodelling. J. Orthop. Res. 8: 651–670
2. Carter DR, Beaupré GS (2001) Skeletal Function and Form – Mechanobiology of Skeletal Development, Aging and Regeneration. Cambridge University Press
3. Carter DR, Hayes WC (1977) The behavior of bone as a two-phase porous structure. J. Bone Jt. Surgery 59-A: 785–794
4. Carter DR, Orr TE, Fhyrie DP (1989) Relationships between loading history and femoral can–cellous bone architecture. J. Biomech. 22: 231–244
5. Chen Y-C, Hoger A (2000) Constitutive functions of elastic materials in finite growth and deformation. J. Elasticity 59: 175–193
6. Cowin SC (1996) Strain or deformation rate dependent finte growth in soft tissues. J. Biomech. 29: 647–649
7. Cowin SC, Arramon YP, Luo GM, Sadegh AM (1998) Remarks on the technical note entitled Temporal stability of node-based internal bone adaption. J. Biomech. 31: 103–104
8. Cowin SC, Hegedus DH (1976) Bone remodelling I: Theory of adaptive elasticity. J. Elasticity 6: 313–326
9. Ehlers W, Markert B (1998) Modellierung fluidgesättigter, viskoelastischer poröser Festkörper in der Biomechanik. In: Die Methode der Finiten Elemente in der Biomechanik, Biomedizin und angrenzenden Gebieten. Workshop 1998, Universität Ulm
10. Epstein M, Maugin GA (2000) Thermomechanics of volumetric growth in uniform bodies. Int. J. Plasticity 16: 951–978
11. Fischer KJ, Jacobs CR, Levenston ME, Carter DR (1997) Observations of convergence and uniqueness of node–based bone remodeling simulations. Annals Biomed. Eng. 25: 261–268
12. Fung YC (1990) Biomechanics – Motion, Flow, Stress, and Growth. Springer Verlag, Berlin – Heidelberg – New York
13. Fung YC (1993) Biomechanics – Mechanical Properties of Living Tissues. Springer Verlag, Berlin – Heidelberg – New York, second edition
14. Gasser TC, Holzapfel GA (2002) A rate-independent elasto-plastic constitutive model for biological fiber-reinforced composites at finite strains: Continuum basis, algorithmic formulation and finite element implementation. Comput. Mech. 29: 340–360
15. Gibson LJ, Ashby MF (1982) The mechanics of three–dimensional cellular materials. Proc Royal Soc London, A 382: 43–59
16. Harrigan TP, Hamilton JJ (1992) An analytical and numerical study of the stability of bone remodelling theories: Dependence on microstructural stimulus. J. Biomech. 25: 477–488. Corrigendum 26: 365–366 (1993)
17. Harrigan TP, Hamilton JJ (1992) Optimality condition for finite element simulation of adaptive bone remodeling. Int. J. Solids Struct. 29: 2897–2906
18. Harrigan TP, Hamilton JJ (1993) Finite element simulation of adaptive bone remodelling: A stability criterion and a time stepping method. Int. J. Numer. Meth. Eng. 36: 837–854
19. Harrigan TP, Hamilton JJ (1994) Necessary and sufficient conditions for global stability and uniqueness in finite element siumlations of adaptive bone remodeling. Int. J. Solids Struct. 31: 97–107
20. Harrigan TP, Hamilton JJ, Reuben JD, Tone A, Viceconti M (1996) Bone remodelling adjcent to intromedullary stems: An optimal structures approach. Biomaterials 17: 223–232
21. Hart RT (2001) Bone modeling and remodeling: Theories and computation. In: Bone Biomechanics Handbook, Cowin SC, (ed.) chapter 31, pp. 1–42. CRC-Press, Boca Raton
22. Holzapfel GA, Gasser TC Ogden RW (2000) A new constitutive framework for arterial wall mechanics and a comparative study of material models. J. Elasticity 61: 1–48
23. Huiskes R (2000) Challenges in Bone Biomechanics. Intree-rede, Technische Universiteit Eindhoven.
24. Huiskes R, Chao EYS (1983) A survey of finite element analysis in orthopedic biomechanics: The first decade. J. Biomech. 16: 385–409
25. Huiskes R, Ruimerman R, van Lenthe GH Janssen JD (1990) Effects of mechanical forces on maintenance and adaption of form in trabecular bone. Nature 405: 704–706
26. Huiskes R, Weinans H, Grootenboer HJ, Dalstra M, Fudala B, Slooff TJ (1987) Adaptive bone–remodeling theory applied to prosthetic–design analysis. J. Biomech. 20: 1135–1150
27. Humphrey JD (2002) Cardiovasular Solid Mechanics. Springer Verlag, Berlin – Heidelberg – New York
28. Jacobs CR, Levenston ME, Beaupré GS, Simo JC, Carter DR (1995) Numerical instabilities in bone remodeling simulations: The advantages of a node–based finite element approach. J. Biomech. 28: 449–459
29. Krstin N, Nackenhorst U, Lammering R (1999). Zur konstitutiven Beschreibung des anisotropen beanspruchungsadaptiven Knochenumbaus. In: Die Methode der Finiten Elemente in der Biomechanik, Biomedizin und angrenzenden Gebieten. Workshop 1999, Universität Ulm
30. Krstin N, Nackenhorst U, Lammering R (2000) Zur konstitutiven Beschreibung des anisotropen beanspruchungs-sadaptiven Knochenumbaus. Technische Mechanik 20: 31–40
31. Kuhl E, Steinmann P (2002) Mass–and volume specific views on thermodynamics for open systems. Proce. Royal Soc. London (Accepted for publication)
32. Kuhl E, Steinmann P (2002) Material forces in open system mechanics. Comput. Meth. Appl. Mech. Eng. (for publication)
33. Kuhl E, Steinmann P (2002) Theory and numerics of geometrically nonlinear open system mechanics. Int. J. Numer. Meth. Eng. (Accepted for publication)
34. Kuhl E, Steinmann P (2003) Computational modeling of healing: An application of the material force method. Biomechanics and Modeling in Mechanobiology, (Accepted for publication)
35. Kuhl E, Steinmann P (2003) On spatial and material settings of thermo-hyperelastodynamics for open systems. Acta Mechanica 160: 179–217

36. **Kühn W, Hauger W** (2000) A theory of adaptive growth of biological materials. Arch. Appl. Mech. 70: 183–192
37. **Levenston ME** (1997) Temporal stability of node-based internal bone adaption simulations. J. Biomech. 30: 403–407
38. **Levenston ME** (1998) Author's response to comments by Cowin et al. regarding Levenston (1997). J. Biomech. 31: 105–106
39. **Levenston ME, Carter DR** (1998) An energy dissipation-based model for damage stimulated bone adaption. J. Biomech. 31: 579–586
40. **Lubarda VA, Hoger A** (2002) On the mechanics of solids with a growing mass. Int. J. Solids Struct. 39: 4627–4664
41. **Mullender MG, Huiskes R** (1995) A proposal for the regulatory mechanisms of Wolff's law. J. Orthop. Res. 13: 503–512
42. **Mullender MG, Huiskes R, Weinans A** (1994) A physiological approach to the simulation of bone remodeling as a self-organizational control process. J. Biomech. 27: 1389–1394
43. **Nackenhorst U** (1997) Ein effizientes Finite Element Verfahren zur Simulation des beanspruchungsadaptiven Knochenwachstums. In: Die Methode der Finiten Elemente in der Biomechanik, Biomedizin und angrenzenden Gebieten. Workshop 1997, Universität Ulm
44. **Nackenhorst U** (1997) Numerical simulations of stress stimulated bone remodeling. Technische Mechanik 17: 31–40
45. **Pauwels** (1965) Gesammelte Abhandlungen zur funktionellen Anatomie des Bewegungsapparates. Springer Verlag, New York – Berlin – Heidelberg
46. **Rodriguez EK, Hoger A, McCulloch AD** (1994) Stress-dependent finite growth in soft elastic tissues. J. Biomechanics 27: 455–467
47. **Steeb H, Diebels S** (2002) A thermodynamic-consistent model describing growth and remodeling phenomena. Comput. Mat. Sci.
48. **Taber LA** (1995) Biomechanics of growth, remodeling, and morphogenesis. ASME Appl. Mech. Rev. 48: 487–545
49. **Weinans H, Huiskes R, Grootenboer HJ** (1992) The behavior of adaptive bone-remodeling simulation models. J. Biomech. 25: 1425–1441
50. **Weinans H, Huiskes R, Grootenboer HJ** (1994) Effects of fit and bonding characteristics of femoral stems on adaptive bone remodeling. J. Biomech. Eng. 116: 393–400
51. **Weinans H, Prendergast PJ** (1996) Tissue adaption as a dynamic process far from equilibrium. Bone 19: 143–149
52. **Weng S** (1997) Ein Evolutionsmodell zur mechanischen Analyse biologischer Strukturen. Dissertation, Mitteilungen aus dem Institut für Mechanik, Ruhr-Universität Bochum, Bochum
53. **Wolff J** (1892) Das Gesetz der Knochentransformation. Hirschwald, Berlin